Pulsewidth Modulation for Electronic Power Conversion

J. Holtz, *Fellow*, IEEE
Wuppertal University – Germany

Abstract – **The efficient and fast control of electric power forms part of the key technologies of modern automated production. It is performed using electronic power converters. The converters transfer energy from a source to a controlled process in a quantized fashion, using semiconductor switches which are turned on and off at fast repetition rates. The algorithms which generate the switching functions – pulsewidth modulation techniques – are manifold. They range from simple averaging schemes to involved methods of real-time optimization. This paper gives an overview.**

1. Introduction

Many three-phase loads require a supply of variable voltage at variable frequency, including fast and high-efficiency control by electronic means. Predominant applications are in variable speed ac drives, where the rotor speed is controlled through the supply frequency, and the machine flux through the supply voltage.

The power requirements for these applications range from fractions of kilowatts to several megawatts. It is preferred in general to take the power from a dc source and convert it to three-phase ac using power electronic dc-to-ac converters. The input dc voltage, mostly of constant magnitude, is obtained from a public utility through rectification, or from a storage battery in the case of an electric vehicle drive.

The conversion of dc power to three-phase ac power is exclusively performed in the switched mode. Power semiconductor switches effectuate temporary connections at high repetition rates between the two dc terminals and the three phases of the ac drive motor. The actual power flow in each motor phase is controlled by the on/off ratio, or duty-cycle, of the respective switches. The desired sinusoidal waveform of the currents is achieved by varying the duty-cycles sinusoidally with time, employing techniques of pulsewidth modulation (PWM).

The basic principle of pulsewidth modulation is characterized by the waveforms in Fig. 1. The voltage waveform

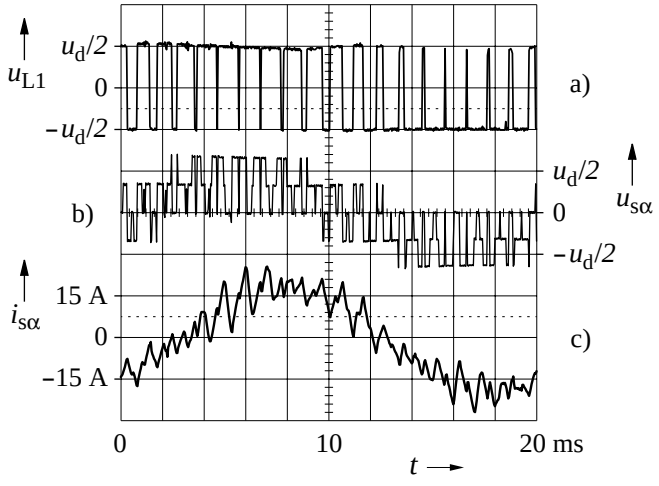

Fig. 1: Recorded three-phase PWM waveforms (suboscillation method); (a) voltage at one inverter terminal, (b) phase voltage $u_{s\alpha}$, (c) load current $i_{s\alpha}$

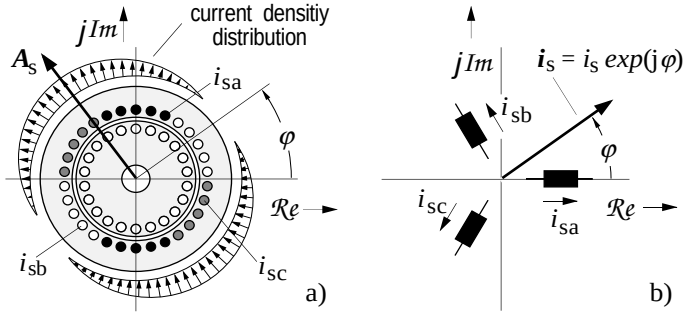

Fig. 2: Definition of a current space vector; (a) cross section of an induction motor, (b) stator windings and stator current space vector in the complex plane

at one inverter terminal, Fig. 1(a), exhibits the varying duty-cycles of the power switches. The waveform is also influenced by the switching in other phases, which creates five distinct voltage levels, Fig. 1(b). Further explanation is given in Section 2.3. The resulting current waveform Fig. 1(c) exhibits the fundamental content more clearly, which is owed to the low-pass characteristics of the machine.

The operation in the switched mode ensures that the efficiency of power conversion is high. The losses in the switch are zero in the off-state, and relatively low during the on-state. There are switching losses in addition which occur during the transitions between the two states. The switching losses increase with switching frequency.

As seen from the pulsewidth modulation process, the switching frequency should be preferably high, so as to attenuate the undesired side-effects of discontinuous power flow at switching. The limitation of switching frequency that exists due to the switching losses creates a conflicting situation. The tradeoff which must be found here is strongly influenced by the respective pulsewidth modulation technique.

Three-phase electronic power converters controlled by pulsewidth modulation have a wide range of applications for dc-to-ac power supplies and ac machine drives. Important quantities to be considered with machine loads are the two-dimensional distributions of current densities and flux linkages in ac machine windings. These can be best analyzed using the space vector approach, to which a short introduction will be given first. Performance criteria will be then introduced to enable the evaluation and comparison of different PWM techniques. The following sections are organized to treat open-loop and closed-loop PWM schemes. Both categories are subdivided into nonoptimal and optimal strategies.

2. An Introduction to Space Vectors

2.1 Definitions

Consider a symmetrical three-phase winding of an electric machine, Fig. 2(a), reduced to a two-pole arrangement for simplicity. The three phase axes are defined by the unity vectors, $\boldsymbol{1}$, $\boldsymbol{a}$, and $\boldsymbol{a}^2$, where $\boldsymbol{a} = exp(2\pi/3)$. Neglecting space harmonics, a sinusoidal current density distribution is es-

tablished around the air-gap by the phase currents i_{sa}, i_{sb}, and i_{sc} as shown in Fig. 2(b). The wave rotates at the angular frequency of the phase currents. Like any sinusoidal distribution in time and space, it can be represented by a complex phasor $\boldsymbol{A}_s$ as shown in Fig. 2(a). It is preferred, however, to describe the mmf wave by the equivalent current phasor $\boldsymbol{i}_s$, because this quantity is directly linked to the three stator currents i_{sa}, i_{sb}, i_{sc} that can be directly measured at the machine terminals:

$$\boldsymbol{i}_s = \frac{2}{3}\left(i_{sa} + \boldsymbol{a}\, i_{sb} + \boldsymbol{a}^2\, i_{sc}\right) \tag{1}$$

The subscript s refers to the stator of the machine.

The complex phasor in (1), more frequently referred to in the literature as a current space vector [1], has the same direction in space as the magnetic flux density wave produced by the mmf distribution $\boldsymbol{A}_s$.

A sinusoidal flux density wave can be also described by a space vector. It is preferred, however, to choose the corresponding distribution of the flux linkage with a particular three-phase winding as the characterizing quantity. For example, we write the flux linkage space vector of the stator winding in Fig. 2 as

$$\boldsymbol{\psi}_s = l_s\, \boldsymbol{i}_s \tag{2}$$

In the general case, when the machine develops nonzero torque, both space vectors $\boldsymbol{i}_s$ of the stator current, and $\boldsymbol{i}_r$ of the rotor current are nonzero, yielding the stator flux linkage vector as

$$\boldsymbol{\psi}_s = l_s\, \boldsymbol{i}_s + l_h\, \boldsymbol{i}_r \tag{3}$$

where l_s is the equivalent stator winding inductance and l_h the composite mutual inductance between the stator and rotor windings. Furthermore,

$$\boldsymbol{i}_r = \frac{2}{3}\left(i_{ra} + \boldsymbol{a}\, i_{rb} + \boldsymbol{a}^2\, i_{rc}\right) \tag{4}$$

is the rotor current space vector, i_{ra}, i_{rb} and i_{rc} are the three rotor currents. Note that flux linkage vectors like $\boldsymbol{\psi}_s$ also represent sinusoidal distributions in space, which can be seen from an inspection of (2) or (3).

The rotating stator flux linkage wave $\boldsymbol{\psi}_s$ generates induced voltages in the stator windings which are described by

$$\boldsymbol{u}_s = \frac{d\boldsymbol{\psi}_s}{dt}, \tag{5}$$

where

$$\boldsymbol{u}_s = \frac{2}{3}\left(u_{sa} + \boldsymbol{a}\, u_{sb} + \boldsymbol{a}^2\, u_{sc}\right) \tag{6}$$

is the space vector of the stator voltages, and u_{sa}, u_{sb}, u_{sc} are the stator phase voltages.

The individual phase quantities associated to any space vector are obtained as the projections of the space vector on the respective phase axis. Given the space vector $\boldsymbol{u}_s$, for example, we obtain the phase voltages as

$$\begin{aligned} u_{sa} &= \mathcal{Re}\{\boldsymbol{u}_s\} \\ u_{sb} &= \mathcal{Re}\left\{\boldsymbol{a}^2 \cdot \boldsymbol{u}_s\right\} \\ u_{sc} &= \mathcal{Re}\{\boldsymbol{a} \cdot \boldsymbol{u}_s\} \end{aligned} \tag{7}$$

Considering the case of three-phase dc-to-ac power supplies, an *LC*-filter and the connected load replace the motor at the inverter output terminals. Although not distributed in space, such load circuit behaves exactly the same way as a motor load. It is permitted and common practice therefore to extend the space vector approach to the analysis of equivalent lumped parameter circuits.

2.2 Normalization

Normalized quantities are used throughout this paper. Space vectors are normalized with reference to the nominal values of the connected ac machine. The respective base quantities are

- the rated peak phase voltage $\sqrt{2}\, U_{ph\,R}$,
- the rated peak phase current $\sqrt{2}\, I_{ph\,R}$, and
- the rated stator frequency ω_{sR}.

(8)

Using the definition of the maximum modulation index in section 4.1.1, the normalized dc bus voltage of a dc link inverter becomes $u_d = \pi/2$.

2.3 Switching state vectors

The space vector resulting from a symmetrical sinusoidal voltage system u_{sa}, u_{sb}, u_{sc} of frequency ω_s is

$$\boldsymbol{u}_s = u_s \cdot \exp(\mathrm{j}\omega_s t), \tag{9}$$

which can be shown by inserting the phase voltages (7) into (6).

A three-phase machine being fed from a switched power converter Fig. 3 receives the symmetrical rectangular three-phase voltages shown in Fig. 4. The three phase potentials Fig. 4(a) are constant over every sixth of the fundamental period, assuming one of the two voltage levels, $+U_d/2$ or $-U_d/2$, at a given time. The neutral point potential u_{np}, Fig. 3, of the load is either positive, when more than one upper half-bridge switch is closed, Fig. 4(b); it is negative with more than one lower half-bridge switch closed. The respective voltage levels shown in Fig. 4(b) hold for symmetrical load impedances.

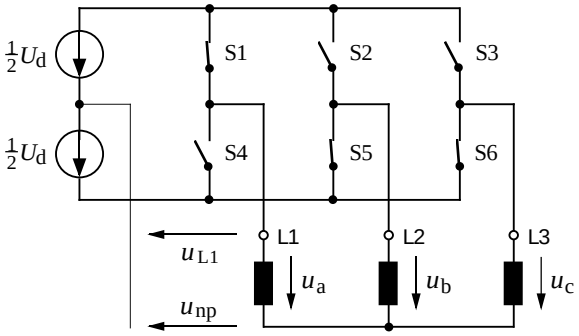

Fig. 3: Three-phase power converter; the switch pairs S1 – S4 (and S2 – S5, and S3 – S6) form half-bridges; one, and only one switch in a half bridge is closed at a time.

The waveform of the phase voltage $u_a = u_{L1} - u_{np}$ is displayed in the upper trace of Fig. 4(c). It forms a symmetrical, nonsinusoidal three-phase voltage system along with the other phase voltages u_b and u_c. Since the waveform u_{np} has three times the frequency of u_{Li}, $i = 1, 2, 3$, while its amplitude equals exactly one third of the amplitudes of u_{Li}, this waveform contains exactly all triplen of the harmonic components of u_{Li}. Because of $u_a = u_{L1} - u_{np}$ there are no triplen harmonics left in the phase voltages. This is also true for the general case of three-phase symmetrical pulsewidth modulated waveforms. As all triplen harmonics form zero-sequence systems, they produce no currents in the machine windings, provided there is no electrical connection to the star-point of the load, i. e. u_{np} in Fig. 3 must not be shorted.

The example Fig. 4 demonstrates also that a change of

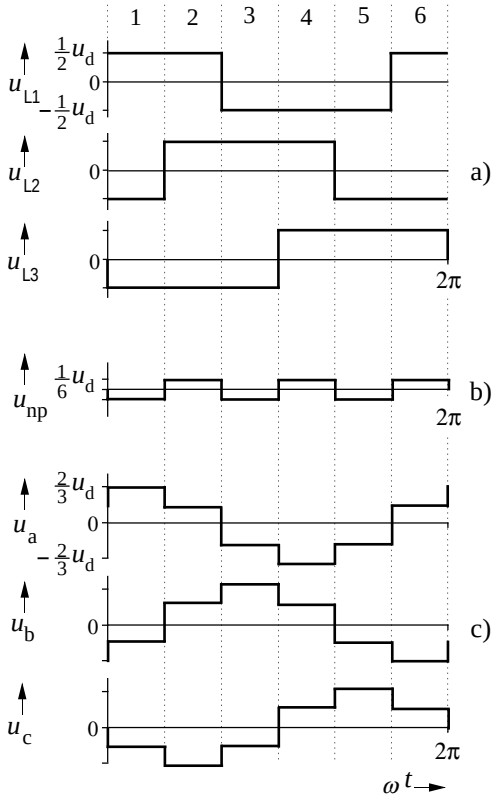

Fig. 4: Switched three-phase waveforms; (a) voltage potentials at the load terminals, (b) neutral point potential, (c) phase voltages

any half-bridge potential invariably influences upon the other two-phase voltages. It is therefore expedient for the design of PWM strategies and for the analysis of PWM waveforms to analyse the three-phase voltages as a whole, instead of looking at the individual phase voltages separately. The space vector approach complies exactly with this requirement.

Inserting the phase voltages Fig. 4(c) into (6) yields the typical set of six active switching state vectors $\boldsymbol{u}_1$ ... $\boldsymbol{u}_6$ shown in Fig. 5. The switching state vectors describe the inverter output voltages.

At operation with pulsewidth modulated waveforms, the two zero vectors $\boldsymbol{u}_0$ and $\boldsymbol{u}_7$ are added to the pattern in Fig. 5. The zero vectors are associated to those inverter states with all upper half-bridge switches closed, or all lower, respectively. The three machine terminals are then short-circuited, and the voltage vector assumes zero magnitude.

Using (7), the three phase voltages of Fig. 4(c) can be reconstructed from the switching state pattern Fig. 5.

3. Performance Criteria

Considering an ac machine drive, it is the leakage inductances of the machine and the inertia of the mechanical system which account for low pass filtering of the harmonic components contained in the switched voltage waveforms. Remaining distortions of the current waveforms, harmonic losses in the power converter and the load, and oscillations in the electromagnetic machine torque are due to the operation in the switched mode. They can be valued by performance criteria [2] ... [7]. These provide the means of comparing the qualities of different PWM methods and support the selection of a pulsewidth modulator for a particular application.

3.1 Current harmonics

The harmonic currents primarily determine the copper losses of the machine, which account for a major portion of the machine losses. The rms harmonic current

$$I_{\text{h rms}} = \sqrt{\frac{1}{T}\int_T [i(t) - i_1(t)]^2\, dt} \tag{10}$$

does not only depend on the performance of the pulsewidth modulator, but also on the internal impedance of the machine. This influence is eliminated when using the distortion factor

$$d = \frac{I_{\text{h rms}}}{I_{\text{h rms six-step}}} \tag{11}$$

as a figure of merit. In this definition, the distortion current I_{hrms} (10) of a given switching sequence is referred to the distortion current $I_{\text{h rms six-step}}$ of same ac load operated in the six-step mode, i. e. with the unpulsed rectangular voltage waveforms Fig. 4(c). The definition (11) values the ac-side current distortion of a PWM method independently from the properties of the load. We have $d = 1$ at six-step operation by definition. Note that the distortion factor d of a pulsed waveform can be much higher than that of a rectangular wave, e. g. Fig. 19.

The harmonic content of a current space vector trajectory is computed as

$$I_{\text{h rms}} = \sqrt{\frac{1}{T}\int_T (\boldsymbol{i}(t) - \boldsymbol{i}_1(t)) \cdot (\boldsymbol{i}(t) - \boldsymbol{i}_1(t))^*\, dt} \tag{12}$$

from which d can be determined by (11). The asterisc in (12) marks the complex conjugate.

The harmonic copper losses in the load circuit are proportional to the square of the harmonic current: $P_{\text{Lc}} \propto d^2$, where d^2 is the loss factor.

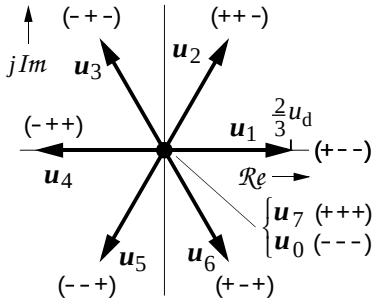

Fig. 5: Switching state vectors in the complex plane; in brackets: switching polarities of the three half-bridges

3.2 Harmonic spectrum

The contributions of individual frequency components to a nonsinusiodal current wave are expressed in a harmonic current spectrum, which is a more detailed description than the global distortion factor d. We obtain discrete current spectra $h_i(k \cdot f_1)$ in the case of synchronized PWM, where the switching frequency $f_s = N \cdot f_1$ is an integral multiple of the fundamental frequency f_1. N is the pulse number, or gear ratio, and k is the order of the harmonic component. Note that all harmonic spectra in this paper are normalized as per the definition (11):

$$h_i(k \cdot f_1) = \frac{I_{\text{h rms}}(k \cdot f_1)}{I_{\text{h rms six-step}}}. \tag{13}$$

They describe the properties of a pulse modulation scheme independently from the parameters of the connected load.

Nonsynchronized pulse sequences produce harmonic am-

plitude density spectra $h_d(f)$ of the currents, which are continuous functions of frequency. They generally contain periodic as well as nonperiodic components and hence must be displayed with reference to two different scale factors on the ordinate axis, e. g. Fig. 35. While the normalized discrete spectra do not have a physical dimension, the amplitude density sprectra are measured in $Hz^{-1/2}$. The normalized harmonic current (11) is computed from the discrete spectrum (13) as

$$d = \sqrt{\sum_{k\neq 1} h_i^2(k\cdot f_1)}\,, \tag{14}$$

and from the amplitude density spectrum as

$$d = \sqrt{\int_{0,\, f\neq f_1}^{\infty} h_d^2(f)\,df}\ . \tag{15}$$

Another figure of merit for a given PWM scheme is the product of the distortion factor and the switching frequency of the inverter. This value can be used to compare different PWM schemes operated at different switching frequencies provided that the pulse number $N > 15$. The relation becomes nonlinear at lower values of N.

3.3 Maximum modulation index

The modulation index is the normalized fundamental voltage, defined as

$$m = \frac{u_1}{u_{1\ \text{six-step}}} \tag{16}$$

where u_1 is the fundamental voltage of the modulated switching sequence and $u_{1\ \text{six-step}} = 2/\pi \cdot u_d$ the fundamental voltage at six-step operation. We have $0 \le m \le 1$, and hence unity modulation index, by definition, can be attained only in the six-step mode.

The maximum value m_{max} of the modulation index may differ in a range of about 25% depending on the respective pulsewidth modulation method. As the maximum power of a PWM converter is proportional to the maximum voltage at the ac side, the maximum modulation index m_{max} constitutes an important utilization factor of the equipment.

3.4 Torque harmonics

The torque ripple produced by a given switching sequence in a connected ac machine can be expressed as

$$\Delta T = (T_{max} - T_{av})/T_R\,, \tag{17}$$

where

T_{max} = maximum air-gap torque,
T_{av} = average air-gap torque,
T_R = rated machine torque.

Although torque harmonics are produced by the harmonic currents, there is no stringent relationship between both of them. Lower torque ripple can go along with higher current harmonics, and vice versa.

3.5 Switching frequency and switching losses

The losses of power semiconductors subdivide into two major portions: The on-state losses

$$P_{on} = g_1(u_{on}, i_L), \tag{18a}$$

and the dynamic losses

$$P_{dyn} = f_s \cdot g_2(U_0, i_L). \tag{18b}$$

It is apparent from (18a) and (18b) that, once the power level has been fixed by the dc supply voltage U_0 and the maximum load current $i_{L\ max}$, the switching frequency f_s is an important design parameter. The harmonic distortion of the ac-side currents reduces almost linearly with this frequency. Yet the switching frequency cannot be deliberately increased for the following reasons:

- The switching losses of semiconductor devices increase proportional to the switching frequency.
- Semiconductor switches for higher power generally produce higher switching losses, and the switching frequency must be reduced accordingly. Megawatt switched power converters using GTO's are switched at only a few 100 hertz.
- The regulations regarding electromagnetic compatibility (EMC) are stricter for power conversion equipment operating at switching frequencies higher than 9 kHz [8].

Another important aspect related to switching frequency is the radiation of acoustic noise. The switched currents produce fast changing electromagnetic fields which exert mechanical Lorentz forces on current carrying conductors, and also produce magnetostrictive mechanical deformations in ferromagnetic materials. It is especially the magnetic circuits of the ac loads that are subject to mechanical excitation in the audible frequency range. Resonant amplification may take place in the active stator iron, being a hollow cylindrical elastic structure, or in the cooling fins on the outer case of an electrical machine.

The dominating frequency components of acoustic radiation are strongly related to the spectral distribution of the harmonic currents and to the switching frequency of the feeding power converter. The psophometric weighting of the human ear makes switching frequencies below 500 Hz and above 10 kHz less critical, while the maximum sensitivity is around 1 - 2 kHz.

3.6 Dynamic performance

Usually a current control loop is designed around a switched mode power converter, the response time of which essentially determines the dynamic performance of the overall system. The dynamics are influenced by the switching frequency and/or the PWM method used. Some schemes require feedback signals that are free from current harmonics. Filtering of feedback signals increases the response time of the loop [10].

PWM methods for the most commonly used voltage-source inverters impress either the voltages, or the currents into the ac load circuit. The respective approach determines the dynamic performance and, in addition, influences upon the structure of the superimposed control system: The methods of the first category operate in an open-loop fashion, Fig. 6(a). Closed-loop PWM schemes, in contrast, inject the currents into the load and require different structures of the control system, Fig. 6(b).

4. Open-loop Schemes

Open-loop schemes refer to a reference space vector $\boldsymbol{u}^*(t)$ as an input signal, from which the switched three-phase voltage waveforms are generated such that the time average of the associated normalized fundamental space vector $\boldsymbol{u}_{s1}(t)$ equals the time average of the reference vector. The general open-loop structure is represented in Fig. 6(a).

4.1 Carrier based PWM

The most widely used methods of pulsewidth modulation are carrier based. They have as a common characteristic subcycles of constant time duration, a subcycle being defined as the time duration $T_0 = 1/2\ f_s$ during which any of the inverter half-bridges, as formed for instance by S1 and S2 in Fig. 3, assumes two consecutive switching states of

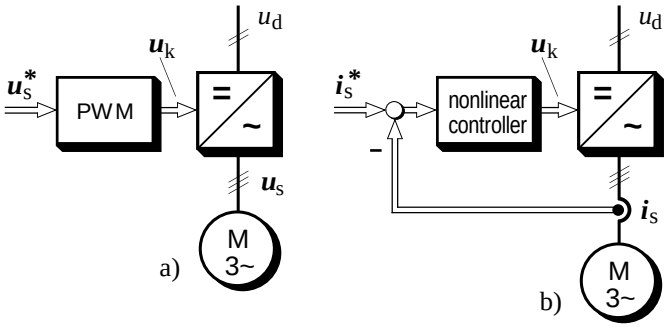

Fig. 6: Basic PWM structures; (a) open-loop scheme, (b) feedback scheme; $\boldsymbol{u}_k$: switching state vector

opposite voltage polarity. Operation at subcycles of constant time duration is reflected in the harmonic spectrum by two salient sidebands, centered around the carrier frequency f_s, and additional frequency bands around integral multiples of the carrier. An example is shown in Fig. 18.

There are various ways to implement carrier based PWM; these which will be discussed next.

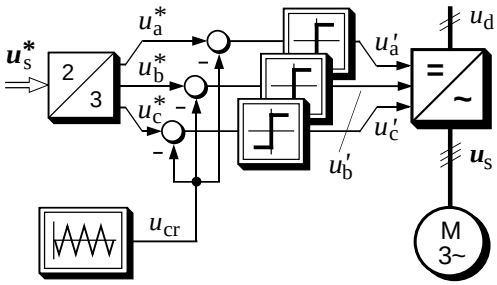

Fig. 7: Suboscillation method; signal flow diagram

4.1.1 Suboscillation method

This method employs individual carrier modulators in each of the three phases [10]. A signal flow diagram is shown in Fig. 7. The reference signals u_a^*, u_b^*, u_c^* of the phase voltages are sinusoidal in the steady-state, forming a symmetrical three-phase system, Fig. 8. They are obtained

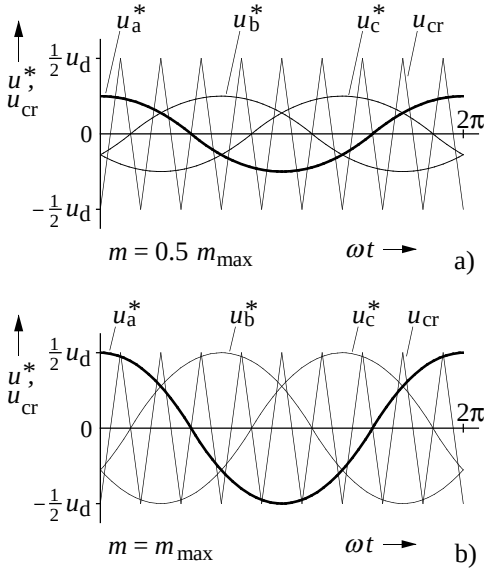

Fig. 8: Reference signals and carrier signal; modulation index (a) $m = 0.5\ m_{max}$, (b) $m = m_{max}$

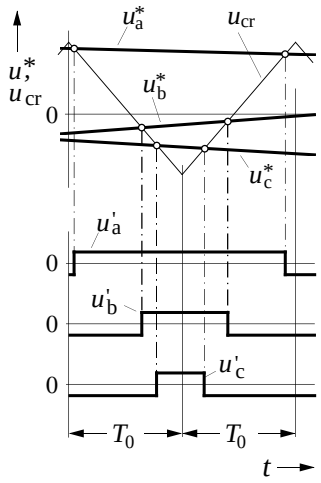

Fig. 9: Determination of the switching instants. T_0: subcycle duration

from the reference vector u^*, which is split into its three phase components u_a^*, u_b^*, u_c^* on the basis of (7). Three comparators and a triangular carrier signal u_{cr}, which is common to all three phase signals, generate the logic signals u'_a, u'_b, and u'_c that control the half-bridges of the power converter.

Fig. 9 shows the modulation process in detail, expanded over a time interval of two subcycles. T_0 is the subcycle duration. Note that the three phase potentials u_a', u_b', u_c' are of equal magnitude at the beginning and at the end of each subcycle. The three line-to-line voltages are then zero, and hence $\boldsymbol{u}_s$ results as the zero vector.

A closer inspection of Fig. 8 reveals that the suboscillation method does not fully utilize the available dc bus voltage. The maximum value of the modulation index $m_{max\,1} = \pi/4 = 0.785$ is reached at a point where the amplitudes of the reference signal and the carrier become equal, Fig. 8(b). Computing the maximum line-to-line voltage amplitude in this operating point yields $u_a^*(t_1) - u_b^*(t_1) = \sqrt{3} \cdot u_d/2 = 0.866\ u_d$. This is less than what is obviously possible when the two half-bridges that correspond to phases *a* and *b* are switched to $u_a = u_d/2$ and $u_b = -u_d/2$, respectively. In this case, the maximum line-to-line voltage amplitude would equal u_d.

Measured waveforms obtained with the suboscillation method are displayed in Fig. 1. This oscillogram was taken at 1 kHz switching frequency and $m \approx 0.75$.

4.1.2 Modified suboscillation method

The deficiency of a limited modulation index, inherent to the suboscillation method, is cured when distorted reference waveforms are used. Such waveforms must not contain other components than zero-sequence systems in addition to the fundamental. The reference waveforms shown in Fig. 10 exhibit this quality. They have a higher fundamental content than sinewaves of the same peak value. As explained in Section 2.3, such distortions are not transferred

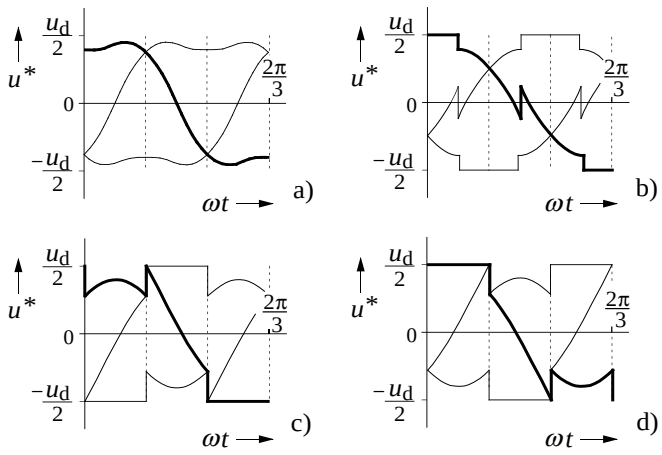

Fig. 10: Reference waveforms with added zero-sequence systems; (a) with added third harmonic, (b), (c), (d) with added rectangular signals of triple fundamental frequency

to the load currents.

There is an infinity of possible additions to the fundamental waveform that constitute zero-sequence systems. The waveform in Fig. 10(a) has a third harmonic content of 25% of the fundamental; the maximum modulation index is increased here to $m_{max} = 0.882$ [11]. The addition of rectangular waveforms of triple fundamental frequency leads to reference signals as shown in Figs. 10(b) through 10(d); $m_{max\,2} = \sqrt{3}\,\pi/6 = 0.907$ is reached in these cases. This is the maximum value of modulation index that can be obtained with the technique of adding zero sequence components to the reference signal [12], [13].

4.1.3 Sampling techniques

The suboscillation method is simple to implement in hardware, using analogue integrators and comparators for the generation of the triangular carrier and the switching instants. Analogue electronic components are very fast, and inverter switching frequencies up to several tens of kilohertz are easily obtained.

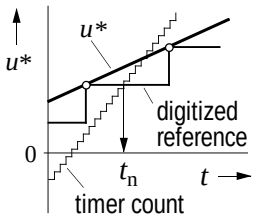

Fig. 11: Natural sampling

When digital signal processing methods based on microprocessors are preferred, the integrators are replaced by digital timers, and the digitized reference signals are compared with the actual timer counts at high repetition rates to obtain the required time resolution. Fig. 11 illustrates this process, which is referred to as natural sampling [14].

To releave the microprocessor from the time consuming task of comparing two time variable signals at a high repetition rate, the corresponding signal processing functions have been implemented in on-chip hardware. Modern microcontrollers comprise of capture/compare units which generate digital control signals for three-phase PWM when loaded from the CPU with the corresponding timing data [15].

If the capture/compare function is not available in hardware, other sampling PWM methods can be employed [16]. In the case of symmetrical regular sampling, Fig. 12(a), the reference waveforms are sampled at the very low repetition rate f_s which is given by the switching frequency. The sampling interval $1/f_s = 2T_0$ extends over two subcycles. t_{sn} are the sampling instants. The triangular carrier shown as a dotted line in Fig. 12(a) is not really existent as a signal. The time intervals T_1 and T_2, which define the switching instants, are simply computed in real time from the respective sampled value $u^*(t_s)$ using the geometrical relationships

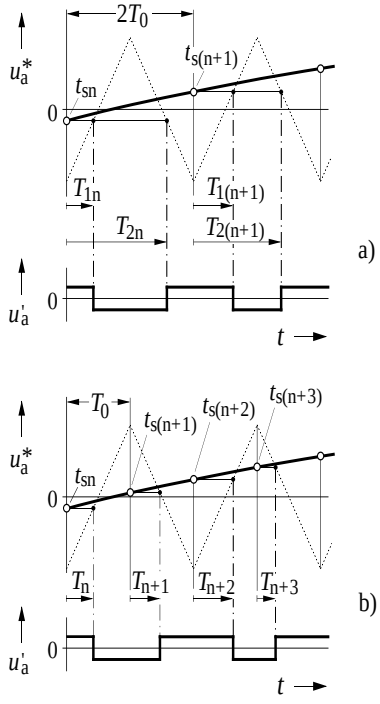

Fig. 12: Sampling techniques; (a) symmetrical regular sampling, (b) asymmetric regular sampling

$$T_1 = \frac{1}{2} T_0 \cdot (1 + u^*(t_s)) \tag{19a}$$

$$T_1 = T_0 + \frac{1}{2} T_0 \cdot (1 - u^*(t_s)) \tag{19b}$$

which can be established with reference to the dotted triangular line.

Another method, referred to as asymmetric regular sampling [18], operates at double sampling frequency $2f_s$. Fig. 12(b) shows that samples are taken once in every subcycle. This improves the dynamic response and produces somewhat less harmonic distortion of the load currents.

4.1.4 Space vector modulation

The space vector modulation technique differs from the aforementioned methods in that there are not separate modulators used for each of the three phases. Instead, the complex reference voltage vector is processed as a whole [18], [19]. Fig. 13(a) shows the principle. The reference vector $\boldsymbol{u}^*$ is sampled at the fixed clock frequency $2f_s$. The sampled value $\boldsymbol{u}^*(t_s)$ is then used to solve the equations

$$2f_s \cdot (t_a \boldsymbol{u}_a + t_b \boldsymbol{u}_b) = \boldsymbol{u}^*(t_s) \tag{20a}$$

$$t_0 = \frac{1}{2f_s} - t_a - t_b \tag{20b}$$

where $\boldsymbol{u}_a$ and $\boldsymbol{u}_b$ are the two switching state vectors adjacent in space to the reference vector $\boldsymbol{u}^*$, Fig. 13(b). The solutions of (20) are the respective on-durations t_a, t_b, and t_0 of the switching state vectors $\boldsymbol{u}_a$, $\boldsymbol{u}_b$, $\boldsymbol{u}_0$:

$$t_1 = \frac{1}{2f_s} \cdot u^*(t_s)\, \frac{3}{\pi} \left(\cos\alpha - \frac{1}{\sqrt{3}} \sin\alpha \right) \tag{21a}$$

$$t_2 = \frac{1}{2f_s} \cdot u^*(t_s)\, \frac{2\sqrt{3}}{\pi} \sin\alpha \tag{21b}$$

$$t_0 = \frac{1}{2f_s} - t_1 - t_2 \tag{21c}$$

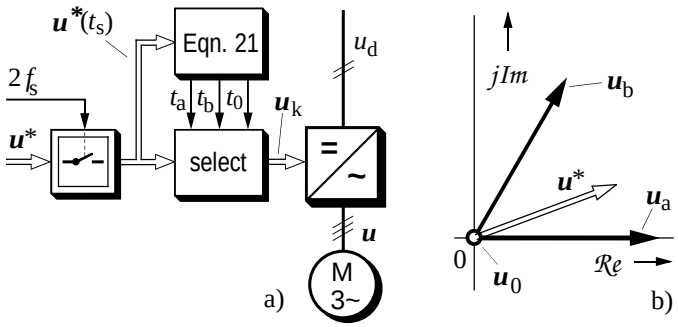

Fig. 13: Space vector modulation; (a) signal flow diagram, (b) switching state vectors of the first 60°-sector

The angle α in these equations is the phase angle of the reference vector.

This technique in effect averages the three switching state vectors over a subcycle interval $T_0 = 1/2f_s$ to equal the reference vector $\boldsymbol{u}^*(t_s)$ as sampled at the beginning of the subcycle. It is assumed in Fig. 13(b) that the reference vector is located in the first 60°-sector of the complex plane. The adjacent switching state vectors are then $\boldsymbol{u}_a = \boldsymbol{u}_1$ and $\boldsymbol{u}_b = \boldsymbol{u}_2$, Fig. 5. As the reference vector enters the next sector, $\boldsymbol{u}_a = \boldsymbol{u}_2$ and $\boldsymbol{u}_b = \boldsymbol{u}_3$, and so on. When programming a microprocessor, the reference vector is first rotated back by $n \cdot 60°$ until it resides in the first sector, and then (21) is

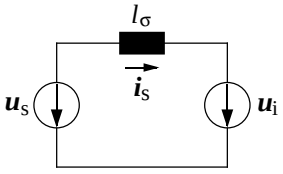

Fig. 14: Induction motor, equivalent circuit

evaluated. Finally, the switching states to replace the provisional vectors $\boldsymbol{u}_a$ and $\boldsymbol{u}_b$ are identified by rotating $\boldsymbol{u}_a$ and $\boldsymbol{u}_b$ forward by $n \cdot 60°$ [20].

Having computed the on-durations of the three switching state vectors that form one subcycle, an adequate sequence in time of these vectors must be determined next. Associated to each switching state vector in Fig. 5 are the switching polarities of the three half-bridges, given in brackets. The zero vector is redundant. It can b either formed as $\boldsymbol{u}_0$ (- - -), or $\boldsymbol{u}_7$ (+ + +). $\boldsymbol{u}_0$ is preferred when the previous switching state vector is $\boldsymbol{u}_1$, $\boldsymbol{u}_3$, or $\boldsymbol{u}_5$; $\boldsymbol{u}_7$ will be chosen following $\boldsymbol{u}_2$, $\boldsymbol{u}_4$, or $\boldsymbol{u}_6$. This ensures that only one half-bridge in Fig. 3 needs to commutate at a transition between an active switching state vector and the zero vector. Hence the minimum number of commutations is obtained by the switching sequence

$$\boldsymbol{u}_0\langle t_0/2\rangle \cdot\cdot \boldsymbol{u}_1\langle t_1\rangle \cdot\cdot \boldsymbol{u}_2\langle t_2\rangle \cdot\cdot \boldsymbol{u}_7\langle t_0/2\rangle \qquad (22a)$$

in any first, or generally in all odd subcycles, and

$$\boldsymbol{u}_7\langle t_0/2\rangle \cdot\cdot \boldsymbol{u}_2\langle t_2\rangle \cdot\cdot \boldsymbol{u}_1\langle t_1\rangle \cdot\cdot \boldsymbol{u}_0\langle t_0/2\rangle \qquad (22b)$$

for the next, or all even subcycles. The notation in (22) associates to each switching state vector its on-duration in brackets.

4.1.5 Modified space vector modulation

The modified space vector modulation [21, 22, 23] uses the switching sequences

$$\boldsymbol{u}_0\langle t_0/3\rangle \cdot\cdot \boldsymbol{u}_1\langle 2t_1/3\rangle \cdot\cdot \boldsymbol{u}_2\langle t_2/3\rangle, \qquad (23a)$$

$$\boldsymbol{u}_2\langle t_2/3\rangle \cdot\cdot \boldsymbol{u}_1\langle 2t_1/3\rangle \cdot\cdot \boldsymbol{u}_0\langle t_0/3\rangle, \qquad (23b)$$

or a combination of (22) and (23). Note that a subcycle of the sequences (23) consists of two switching states, since the last state in (23(a)) is the same as the first state in (23(b)). Similarly, a subcycle of the sequences (22) comprises three switching states. The on-durations of the switching state vectors in (23) are consequently reduced to 2/3 of those in (22) in order to maintain the switching frequency f_s at a given value.

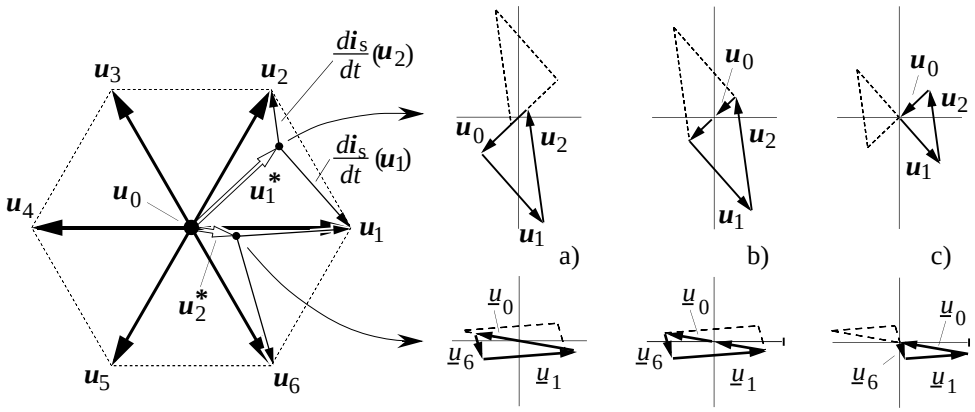

Fig. 15: Linearized trajectories of the harmonic current for two voltage references $\boldsymbol{u}_1$* and $\boldsymbol{u}_2$*: and (a) suboscillation method, (b) space vector modulation, (c) modified space vector modulation

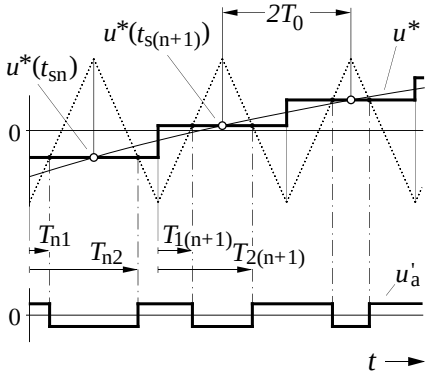

Fig. 16: Synchronized regular sampling

The choice between the two switching sequences (22) and (23) should depend on the value of the reference vector. The decision is based on the analysis of the resulting harmonic current. Considering the equivalent circuit Fig. 14, the differential equation

$$\frac{d\boldsymbol{i}_s}{dt} = \frac{1}{l_\sigma}(\boldsymbol{u}_s - \boldsymbol{u}_i) \qquad (24)$$

can be used to compute the trajectory in space of the current space vector $\boldsymbol{i}_s$. $\boldsymbol{u}_s$ is the actual switching state vector. If the trajectories $d\boldsymbol{i}_s(\boldsymbol{u}_s)/dt$ are approximated as linear, the closed patterns of Fig. 15 will result. The patterns are shown for the switching state sequences (22) and (23), and two different magnitude values, $\boldsymbol{u}_1$* and $\boldsymbol{u}_2$*, of the reference vector are considered. The harmonic content of the trajectories is determined using (12). The result can be confirmed just by a visual inspection of the patterns in Fig. 15: the harmonic content is lower at high modulation index with the modified switching sequence (23); it is lower at low modulation index when the sequence (22) is applied.

Fig. 17 shows the corresponding characteristics of the loss factor d^2: curve svm corresponds to the sequence (22), and curve (c) to sequence (23). The maximum modulation index extends in either case up to $m_{max2} = 0.907$.

4.1.6 Synchronized carrier modulation

The aforementioned methods operate at constant carrier frequency, while the fundamental frequency is permitted to vary. The switching sequence is then nonperiodic in principle, and the corresponding Fourier spectra are continuous. They contain also frequencies lower than the lowest carrier sideband, Fig. 18. These subharmonic components are undesired as they produce low-frequency torque harmonics. A synchronization between the carrier frequency and the controling fundamental avoids these drawbacks which are especially prominent if the frequency ratio, or pulse number

$$N = \frac{f_s}{f_1} \qquad (25)$$

is low. In synchronized PWM, the pulse number N assumes only integral values [24].

When sampling techniques are employed for synchronized carrier modulation, an advantage can be drawn from the fact that the sampling instants $t_{sn} = n/(f_1 \cdot N)$, $n = 1 \ldots N$ in a fundamental peri-

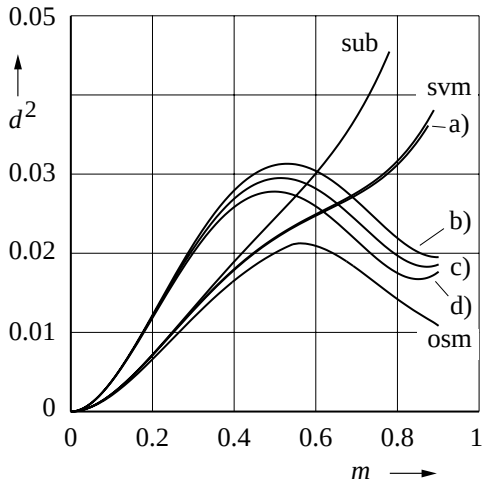

Fig. 17: Performance of carrier modulation at f_s = 2 kHz; for (a) through (d) refer to Fig. 9; sub: suboscillation method, svm: space vector modulation, osm: optimal subcycle method

od are a priori known. The reference signal is $u^*(t) = m/m_{max} \cdot sin\ 2\pi f_1 t$, and the sampled values $u^*(t_s)$ in Fig. 16 form a discretized sine function that can be stored in the processor memory. Based on these values, the switching instants are computed on-line using (19).

4.1.7 Performance of carrier based PWM

The loss factor d^2 of suboscillation PWM depends on the zero-sequence components added to the reference signal. A comparison is made in Fig. 17 at 2 kHz switching frequency. Letters (a) through (d) refer to the respective reference

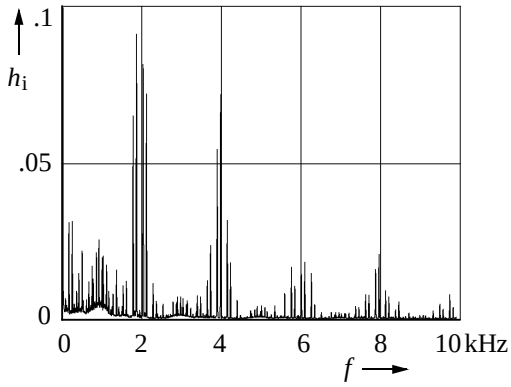

Fig. 18: Space vector modulation, harmonic spectrum

waveforms in Fig. 10.

The space vector modulation exhibits a better loss factor characteristic at $m > 0.4$ as the suboscillation method with sinusoidal reference waveforms. The reason becomes obvious when comparing the harmonic trajectories in Fig. 15. The zero vector appears twice during two subsequent subcycles, and there is a shorter and a subsequent larger portion of it in a complete harmonic pattern of the suboscillation method. Fig. 9 shows how the two different on-durations of the zero vector are generated. Against that, the on-durations of two subsequent zero vectors Fig. 15(b) are basically equal in the case of space vector modulation. The contours of the harmonic pattern come closer to the origin in this case, which reduces the harmonic content.

The modified space vector modulation, curve (d) in Fig. 17, performs better at higher modulation index, and worse at $m < 0.62$.

A typical harmonic spectrum produced by the space vector modulation is shown in Fig. 18.

The loss factor curves of synchronized carrier PWM are shown in Fig. 19 for the suboscillation technique and the space vector modulation. The latter appears superior at low pulse numbers, the difference becoming less significant as N increases. The curves exhibit no differences at lower modulation index. Operating in this range is of little practical use for constant v/f_1 loads where higher values of N are permitted and, above all, d^2 decreases if m is reduced (Fig. 17).

The performance of a pulsewidth modulator based on sampling techniques is slightly inferior than that of the suboscillation method, but only at low pulse numbers.

Because of the synchronism between f_1 and f_s, the pulse number must necessarily change as the modulation index varies over a broader range. Such changes introduce discontinuities to the modulation process. They generally originate current transients, especially when the pulse number is low [25]. This effect is discussed in Section 5.2.3.

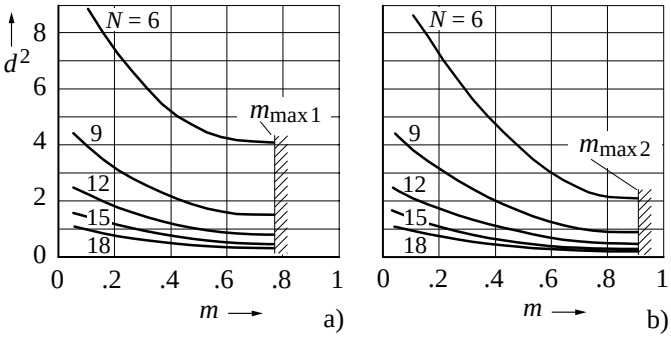

Fig. 19: Synchronized carrier modulation, loss factor d^2 versus modulation index; (a) suboscillation method, (b) space vector modulation

4.2 Carrierless PWM

The typical harmonic spectrum of carrier based pulsewidth modulation exhibits prominent harmonic amplitudes around the carrier frequency and its harmonics, Fig. 18. Increased acoustic noise is generated by the machine at these frequencies through the effects of magnetostriction. The vibrations can be amplified by mechanical resonances. To reduce the mechanical excitation at particular frequencies it may be preferable to have the harmonic energy distributed over a larger frequency range instead of being concentrated around the carrier frequency.

This concept is realized by varying the carrier frequency in a randomly manner. Applying this to the suboscillation technique, the slopes of the triangular carrier signal must be maintained linear in order to conserve the linear input-output relationship of the modulator. Fig. 20 shows how a random frequency carrier signal can be generated. Whenever the carrier signal reaches one of its peak values, its slope is reversed by a hysteresis element, and a sample is taken

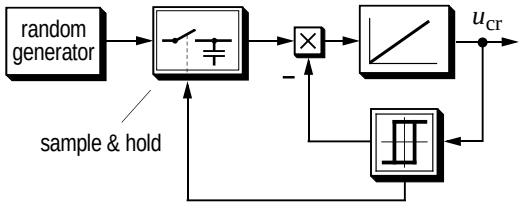

Fig. 20: Random frequency carrier signal generator

from a random signal generator which imposes an additional small variation on the slope. This varies the durations of the subcycles randomly [26]. The average switching frequency is maintained constant such that the power devices are not exposed to changes in temperature.

The optimal subcycle method (Section 6.4.3) classifies also as carrierless. Another approach to carrierless PWM is explained in Fig. 21; it is based on the space vector modulation principle. Instead of operating at constant sampling frequency $2f_s$ as in Fig. 13(a), samples of the reference vector are taken whenever the duration t_{act} of the switching state vector $\boldsymbol{u}_{act}$ terminates. t_{act} is determined from the solution of

$$t_{act}\boldsymbol{u}_{act} + t_1\boldsymbol{u}_1 + \left(\frac{1}{2f_s} - t_{act} - t_1\right)\boldsymbol{u}_2 = \frac{1}{2f_s}\cdot\boldsymbol{u}^*(t), \qquad (26)$$

where $\boldsymbol{u}^*(t)$ is the reference vector. This quantity is different from its time discretized value $\boldsymbol{u}^*(t_s)$ used in 12(a). As $\boldsymbol{u}^*(t)$ is a continuously time-variable signal, the on-durations t_1, t_2, and t_0 are different from the values (20), which introduces the desired variations of subcycle lengths. Note that t_1 is another solution of (26), which is disregarded. The switching state vectors of a subcycle are shown in Fig. 21(b). Once the on-time t_{act} of $\boldsymbol{u}_{act}$ has elapsed, $\boldsymbol{u}_a$ is chosen as $\boldsymbol{u}_{act}$ for the next switching interval, $\boldsymbol{u}_b$ becomes $\boldsymbol{u}_a$, and the cyclic process starts again [27].

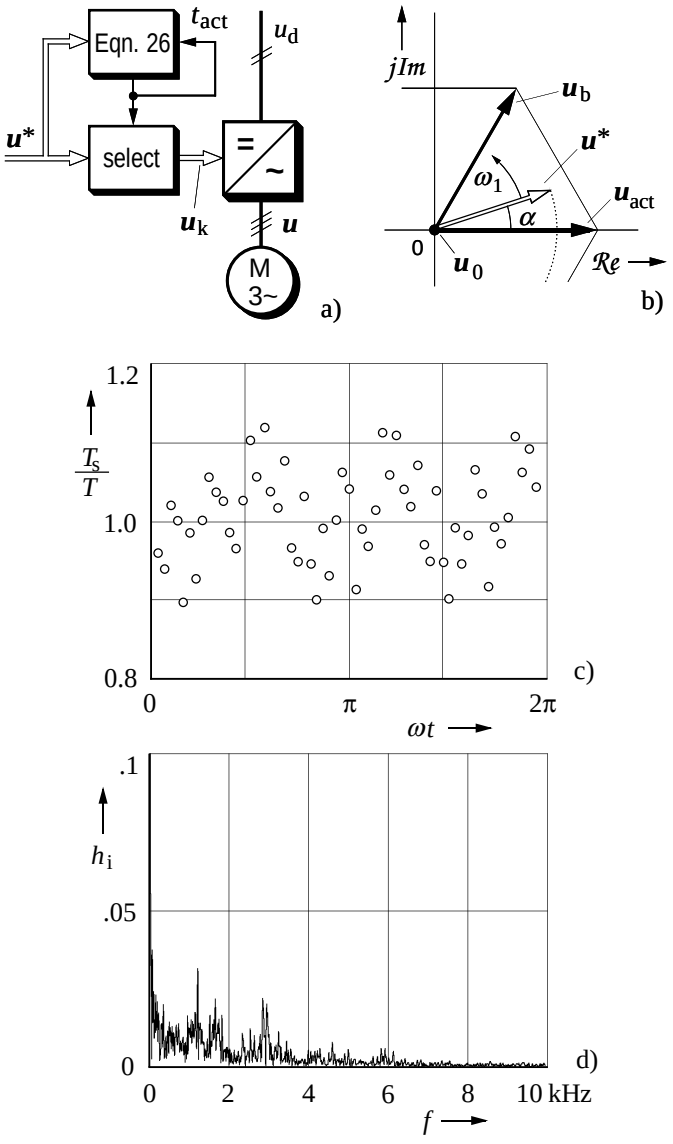

Fig. 21: Carrierless pulsewidth modulation; (a) signal flow diagram, (b) switching state vectors of the first 60°-sector, (c) measured subcycle durations, (d) harmonic spectrum

Fig. 21(c) gives an example of measured subcycle durations in a fundamental period. The comparison of the harmonic spectra Fig. 21(d) and Fig. 18 demonstrates the absence of pronounced spectral components in the harmonic current.

Carrierless PWM equalizes the spectral distribution of the harmonic energy. The energy level is not reduced. To lower the audible excitation of mechanical resonances is a promising aspect. It remains difficult to decide, though, wheather a clear, single tone is better tolerable in its annoying effect than the radiation of white noise.

4.3 Overmodulation

It is apparent from the averaging approach of the space vector modulation technique that the on-duration t_0 of the zero vector $\boldsymbol{u}_0$ (or $\boldsymbol{u}_7$) decreases as the modulation index m increases. $t_0 = 0$ is first reached at $m = m_{max\,2}$, which means that the circular path of the reference vector $\boldsymbol{u}^*$ touches the outer hexagon that is opened up by the switching state vectors Fig. 22(a). The controllable range of linear modulation methods terminates at this point.

An additional singular operating point exists in the six-step mode. It is characterized by the switching sequence u_1 - u_2 - u_3 - ... - u_6 and the highest possible fundamental output voltage corresponding to $m = 1$.

Control in the intermediate range $m_{max\,2} < m < 1$ can be achieved by overmodulation [28]. It is expedient to consider a sequence of output voltage vectors $\boldsymbol{u}_k$, averaged over a subcycle to become a single quantity $\boldsymbol{u}_{av}$, as the characteristic variable. Overmodulation techniques subdivide into two different modes. In mode I, the trajectory of the average voltage vector $\boldsymbol{u}_{av}$ follows a circle of radius $m > m_{max\,2}$ as long as the circle arc is located within the hexagon; $\boldsymbol{u}_{av}$

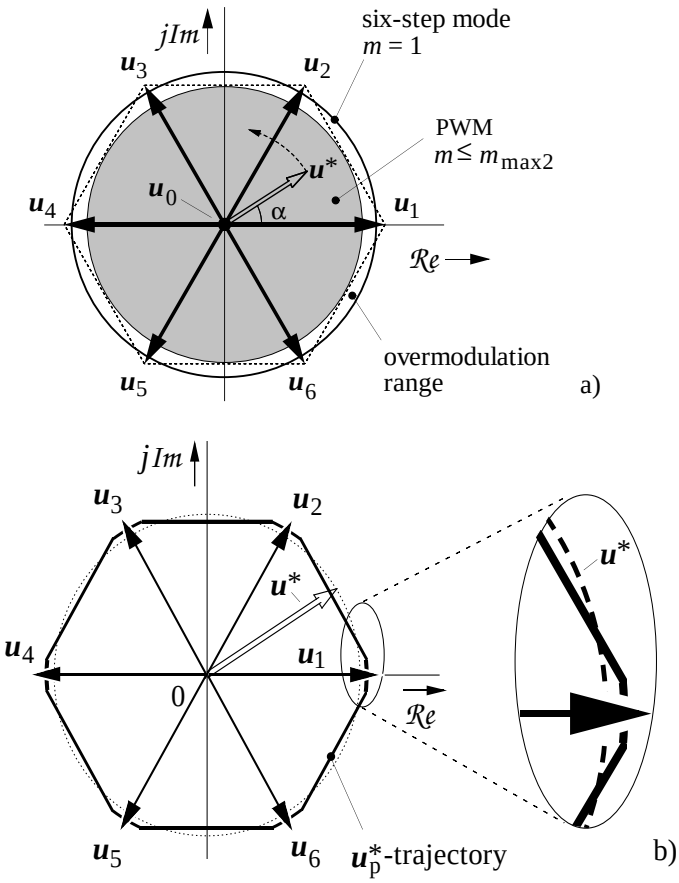

Fig. 22: Overmodulation; (a) definition of the overmodulation range, (b) trajectory of u_{av} in overmodulation range I

tracks the hexagon sides in the remaining portions (Fig. 22(b)). Equations (21) are used to derive the switching durations while $\boldsymbol{u}_{av}$ is on the arc. On the hexagon sides, the durations are $t_0 = 0$ and

$$t_a = T_0 \frac{\sqrt{3}\cos\alpha - \sin\alpha}{\sqrt{3}\cos\alpha + \sin\alpha}, \qquad (27a)$$

$$t_b = T_0 - t_a. \qquad (27b)$$

Overmodulation mode II is reached at $m > m_{max\,3} = 0.952$ when the length of the arcs reduces to zero and the trajectory of $\boldsymbol{u}_{av}$ becomes purely hexagonal. In this mode, the velocity of the average voltage vector is controlled along its linear trajectory by varying the duty cycle of the two switching state vectors adjacent to u_{av}. As m increases, the velocity becomes gradually higher in the center portion of the hexagon side, and lower near the corners. Overmodulation mode II converges smoothly into six-step operation when the velocity on the edges becomes infinite, the velocity at the corners zero.

In mode II a subcycle is made up by only two switching state vectors. These are the two vectors that define the hexagon side on which $\boldsymbol{u}_{av}$ is traveling. Since the switching frequency is normally maintained at constant value, the subcycle duration T_0 must reduce due to the reduced number of switching state vectors. This explaines why the distortion factor reduces at the beginning of the overmodulation range (Fig. 23).

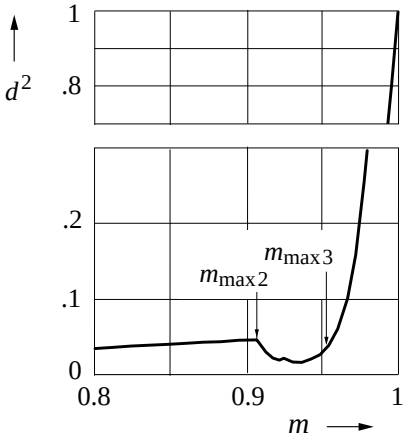

Fig. 23: Loss factor d^2 at overmodulation (different d^2 scales)

The current waveforms Fig. 24 demonstrate that the modulation index is increased beyond the limit existing at linear modulation by the addition of harmonic components to the average voltage u_{av}. The added harmonics do not form zero-sequence components as those discussed in Section 4.1.2. Hence they are fully reflected in the current waveforms, which classifies overmodulation as a nonlinear technique.

4.4 Optimized Open-loop PWM

PWM inverters of higher power rating are operated at very low switching frequency to reduce the switching losses. Values of a few 100 Hertz are customary in the megawatt range. If the choice is a open-loop technique, only synchronized pulse schemes should be employed here in order to avoid the generation of excessive subharmonic components. The same applies for drive systems operating at high fundamental frequency while the switching frequency is in the lower kilohertz range. The pulse number (25) is low in both cases. There are only a few switching instants t_k per fundamental period, and small variations of the respective switching angles $\alpha_k = 2\pi f_1 \cdot t_k$ have considerable influence on the harmonic distortion of the machine currents.

It is advantageous in this situation to determine the finite number of switching angles per fundamental period by optimization procedures. Necessarily the fundamental frequency must be considered constant for the purpose of defining the optimization problem. A solution can be then obtained

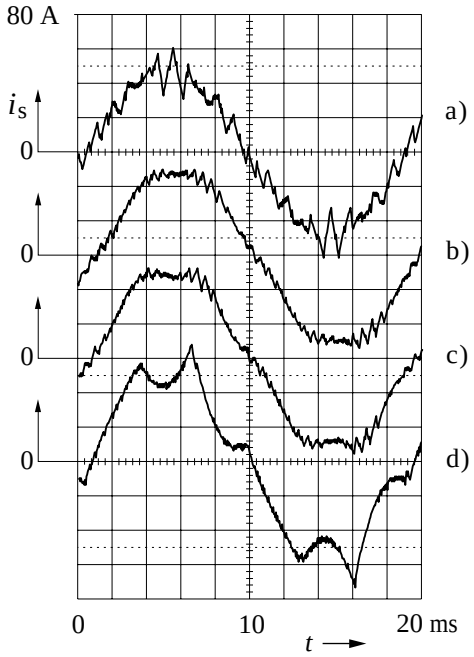

Fig. 24: Current waveforms at overmodulation; (a) space vector modulation at $m_{max\,2}$, (b) transition between range I and range II, (c) overmodulation range II, (d) operation close to the six-step mode

off-line. The precalculated optimal switching patterns are stored in the drive control system to be retrieved during operation in real-time [29].

The application of this method is restricted to quasi steady-state operating conditions. Operation in the transient mode produces waveform distortions worse than with nonoptimal methods (Section 5.2.3).

The best optimization results are achieved with switching sequences having odd pulse numbers and quarter-wave symmetry. Off-line schemes can be classified with respect to the optimization objective [30].

4.4.1 Harmonic elimination

This technique aims at the elimination of a well defined number $n_1 = (N - 1)/2$ of lower order harmonics from the discrete Fourier spectrum. It eliminates all torque harmonics having 6 times the fundamental frequency at $N = 5$, or 6 and 12 times the fundamental frequency at $N = 7$, and so on [31]. The method can be applied when specific harmonic frequencies in the machine torque must be avoided in order to prevent resonant excitation of the driven mechanical system (motor shaft, couplings, gears, load). The approach is suboptimal as regards other performance criteria.

4.4.2 Objective functions

An accepted approach is the minimization of the loss factor d^2 [32], where d is defined by (11) and (14). Alternatively, the highest peak value of the phase current can be considered a quantity to be minimized at very low pulse numbers [33]. The maximum efficiency of the inverter/machine system is another optimization objective [34].

The objective function that defines a particular optimization problem tends to exhibit a very large number of local minimums. This makes the numerical solution extremely time consuming, even on today's modern computers. A set of switching angles which minimize the harmonic current ($d \rightarrow$ min) is shown in Fig. 25.

Fig. 26 compares the performance of a $d \rightarrow min$ scheme at 300 Hz switching frequency with the suboscillation method and the space vector modulation method.

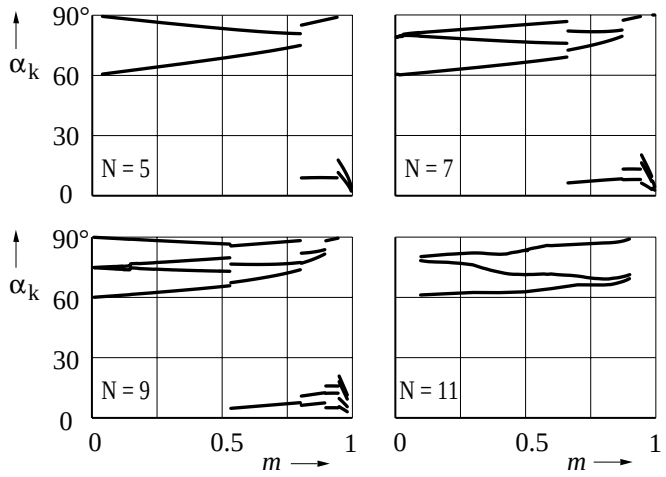

Fig. 25: Optimal switching angles; *N*: pulse number

4.4.3 Optimal Subcycle Method

This method considers the durations of switching subcycles as optimization variables, a subcycle being the time sequence of three consecutive switching state vectors. The sequence is arranged such that the instantaneous distortion current equals zero at the beginning and at the end of the subcycle. This enables the composition of the switched waveforms from a precalculated set of optimal subcycles in any desired sequence without causing undesired current transients under dynamic operating conditions. The approach eliminates a basic deficiency of the optimal pulsewidth modulation techniques that are based on precalculated switching angles [35].

A signal flow diagram of an optimal subcycle modulator

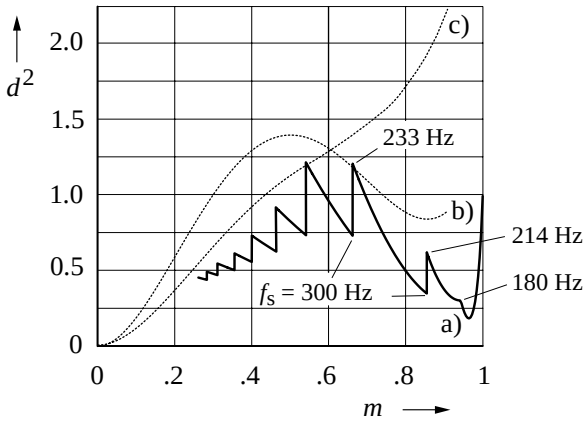

Fig. 26: Loss factor d^2 of synchronous optimal PWM, curve (a); for comparison at f_s = 300 Hz: (b) space vector modulation, (c) suboscillation method

is shown in Fig. 27(a). Samples of the reference vector $\boldsymbol{u}^*$ are taken at $t = t_s$, whenever the previous subcycle terminates. The time duration $T_s(\boldsymbol{u}^*)$ of the next subcycle is then read from a table which contains off-line optimized data as displayed in Fig. 27(b). The curves show that the subcycles enlarge as the reference vector comes closer to one of the active switching state vectors, both in magnitude as in phase angle. This implies that the optimization is only worthwhile in the upper modulation range.

The modulation process itself is based on the space vector approach, taking into account that the subcycle length is variable. Hence T_s replaces $T_0 = 1/2\,f_s$ in (21). A predicted value $\boldsymbol{u}^*(t_s + 1/2\,T_s(\boldsymbol{u}^*(t_s))$ is used to determine the on-times. The prediction assumes that the fundamental frequency does

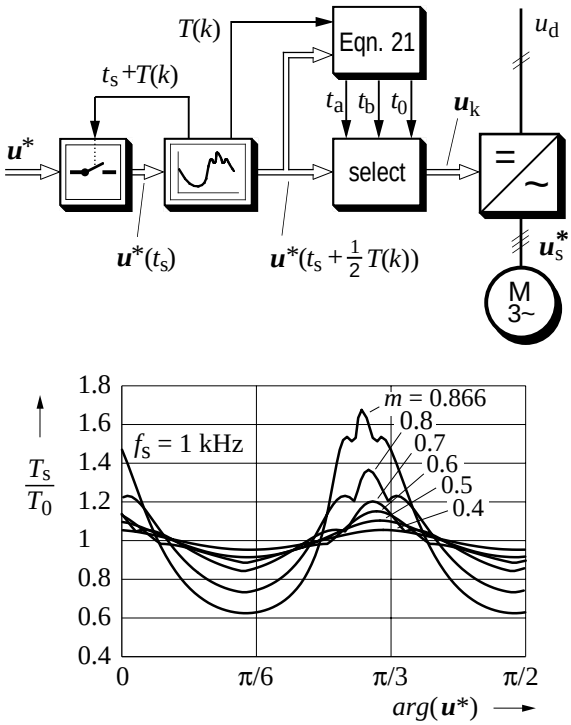

Fig. 27: Optimal subcycle PWM; (a) signal flow diagram, (b) subcycle duration versus fundamental phase angle

not change during a subcycle. It eliminates the perturbations of the fundamental phase angle that would result from sampling at variable time intervals.

The performance of the optimal subcycle method is compared with the space vector modulation technique in Fig. 28. The Fourier spectrum lacks dominant carrier frequencies, which reduces the radiation of acoustic noise from connected loads.

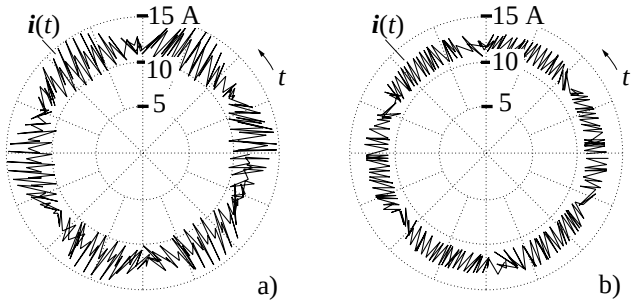

Fig. 28: Current trajectories; (a) space vector modulation, (b) optimal subcycle modulation

4.5 Switching conditions

It was assumed until now that the inverter switches behave ideally. This is not true for almost all types of semiconductor switches. The devices react delayed to their control signals at turn-on and turn-off. The delay times depend on the type of semiconductor, on its current and voltage rating, on the controling waveforms at the gate electrode, on the device temperature, and on the actual current to be switched.

4.5.1 Minimum duration of switching states

In order to avoid unnecessary switching losses of the devices, allowance must be made by the control logic for minimum time durations in the on-state and the off-state, respectively. An additional time margin must be included

so as to allow the snubber circuits to energize or deenergize. The resulting minimum on-duration of a switching state vector is of the order 1 - 100 μs. If the commanded value in an open-loop modulator is less than the required minimum, the respective switching state must be either extended in time or skipped (pulse dropping [36]). This causes additional current waveform distortions, and also constitutes a limitation of the maximum modulation index. The overmodulation techniques described in Section 4.3 avoid such limitations.

4.5.2 Dead-time effect

Minority-carrier devices in particular have their turn-off delayed owing to the storage effect. The storage time T_{st} varies with the current and the device temperature. To avoid short-circuits of the inverter half-bridges, a lock-out time T_d must be introduced by the inverter control. The lock-out time counts from the time instant at which one semiconductor switch in a half-bridge turns off and terminates when the opposite switch is turned on. The lock-out time T_d is determined as the maximum value of storage time T_{st} plus an additional safety time interval.

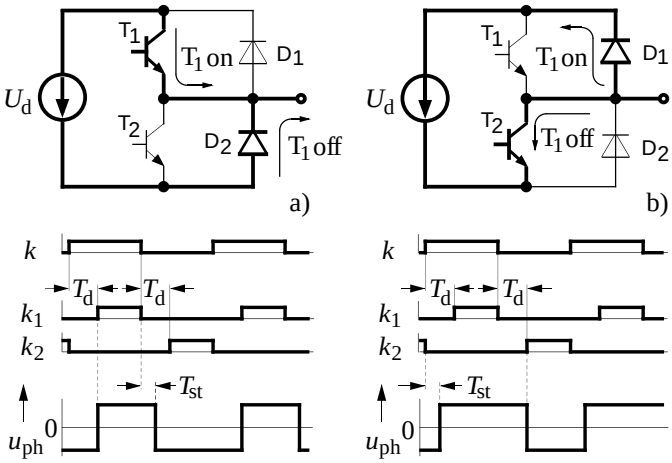

Fig. 29: Inverter switching delay; (a) positive load current, (b) negative load current

We have now two different situations, displayed in Fig. 29(a) for positive load current in a bridge leg. When the modulator output signal k goes high, the base drive signal k_1 of T1 gets delayed by T_d, and so does the reversal of the phase voltage u_{ph}. If the modulator output signal k goes low, the base drive signal k_1 is immediately made zero, but the actual turn-off of T1 is delayed by the device storage time $T_{st} < T_d$. Consequently, the on-time of the upper bridge arm does not last as long as commanded by the controling signal k. It is decreased by the time difference $T_d - T_{st}$, [37].

A similar effect occurs at negative current polarity. Fig. 29(b) shows that the on-time of the upper bridge arm is now increased by $T_d - T_{st}$. Hence, the actual duty cycle of the half-bridge is always different from that of the controlling signal k. It is either increased or decreased, depending on the load current polarity. The effect is described by

$$\boldsymbol{u}_{av} = \boldsymbol{u}^* - \boldsymbol{\Delta u}; \qquad \boldsymbol{\Delta u} = \frac{T_d - T_{st}}{T_s}\, \boldsymbol{sig}\, \boldsymbol{i}_s, \tag{28}$$

where $\boldsymbol{u}_{av}$ is the inverter output voltage vector averaged over a subcycle, and $\boldsymbol{\Delta u}$ is a normalized error vector attributed to the switching delay of the inverter. The error magnitude $\boldsymbol{\Delta u}$ is proportional to the actual safety time margin $T_d - T_{st}$; its direction changes in discrete steps, depending on the respective polarities of the three phase currents. This is expressed in (28) by a polarity vector of constant magnitude

$$\boldsymbol{sig}\, \boldsymbol{i}_s = \frac{2}{3}\left[sign(\boldsymbol{i}_{sa}) + \boldsymbol{a}\cdot sign(\boldsymbol{i}_{sb}) + \boldsymbol{a}^2\cdot sign(\boldsymbol{i}_{sc})\right], \tag{29}$$

where $\boldsymbol{a} = exp(j2\pi/3)$ and $\boldsymbol{i}_s$ is the current vector. The notation $\boldsymbol{sig}(\boldsymbol{i}_s)$ was chosen to indicate that this complex nonlinear function exhibits properties of a sign function. The graph $\boldsymbol{sig}(\boldsymbol{i}_s)$ is shown in Fig. 30(a) for all possible values of the current vector $\boldsymbol{i}_s$. The three phase currents are denoted as i_{as}, i_{bs}, and i_{cs}.

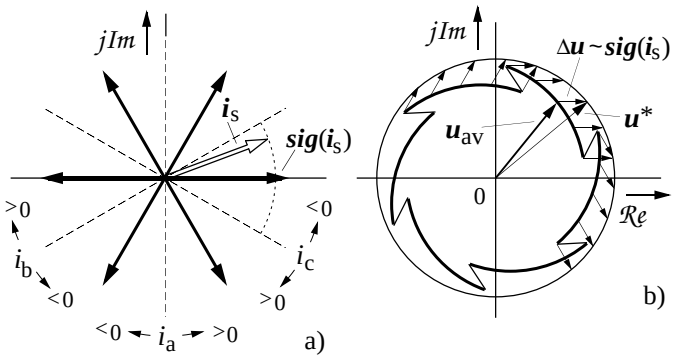

Fig. 30: Dead-time effect; (a) location of the polarity vector $\boldsymbol{sig}(\boldsymbol{i})$, (b) trajectory of the distorted average voltage u_{av}

The dead-time effect described by (28) and (29) produces a nonlinear distortion of the average voltage vector trajectory $\boldsymbol{u}_{av}$. Fig. 30(b) shows an example. The distortion does not depend on the magnitude u_1 of the fundamental voltage and hence its relative influence is very strong in the lower speed range where u_1 is small. Since the fundamental frequency is low in this range, the smoothing action of the load circuit inductance has little effect on the current waveforms, and the sudden voltage changes become clearly visible, Fig. 31(a). The machine torque is influenced as well, exhibiting dips in magnitude at six times the fundamental frequency in the steady-state. Electromechanical stability problems may result if this frequency is sufficiently low. Such case is illustrated in Fig. 32, showing one phase current and the speed signal in permanent instability.

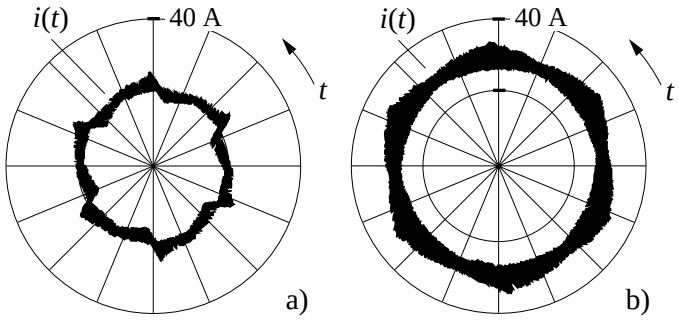

Fig. 31: Dead-time effect; (a) measured current trajectory with sixth harmonic and reduced fundamental, (b) as in (a), with dead-time compensation

4.5.3 Dead-time compensation

If the pulsewidth modulator and the inverter form part of a superimposed high-bandwidth current control loop, the current waveform distortions caused by the dead-time effect are compensated to a certain extent. This may elimi-

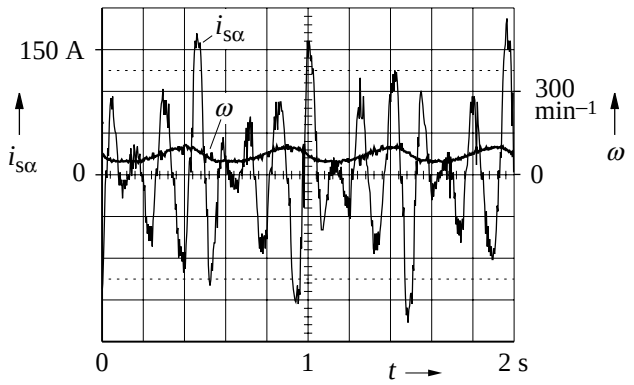

Fig. 32: Electromechanical instability due to the dead-time effect

nate the need for a separate dead-time compensator. A compensator is required when fast current control is not available, or when the machine torque must be very smooth. Dead-time compensators can be implemented in hardware or in software.

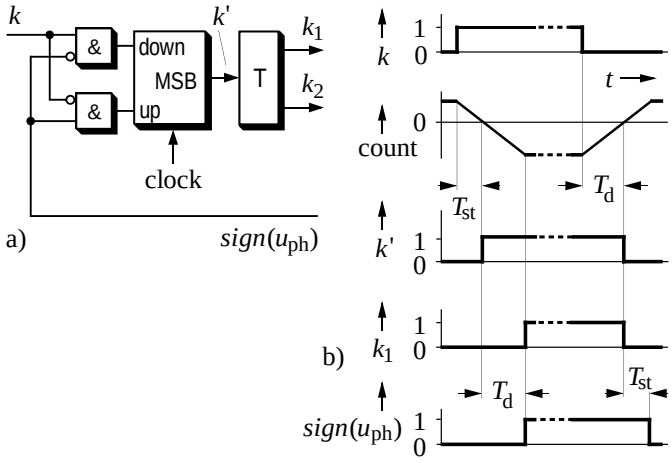

Fig. 33: Dead-time compensation; (a) compensation and delay circuit per phase, (b) signal waveforms; T: interlock circuit

The hardware compensator Fig. 33(a) operates by closed-loop control [38]. Identical circuits are provided for each bridge leg. Each compensator forces a constant time delay between the logic output signal k of the pulse modulator and the actual switching instant. To achieve this, the instant at which the phase voltage changes is measured at the inverter output. A logic signal $sign(u_{ph})$ is obtained that is fed back to control an up-down counter, which in turn controls the bridge: A positive count controls a negative phase voltage, and *vice versa*.

Fig. 33(b) shows the signals at positive load current. The half-bridge output is negative at the beginning, and $sign(u_{ph}) = 0$. The counter holds the measured storage time T_{st} of the previous commutation. It starts downcounting at fixed clock rate when the modulator output k turns high. The inverter control logic receives the on-signal k after T_{st}, and then inserts the lockout time T_d before k_1 turns the bridge on. The total time delay of the turn-on process amounts to $T_d + T_{st}$, and an identical delay is provided for the turn-off process. The switching sequence gets delayed in time, but its duty-cycle is conserved.

When T_{st} changes following a change of the current polarity, the initial count of T_{st} is wrongly set, and the next commutation gets displaced. Thereafter, the duty-cycle is again maintained as the counter starts with a revised value of T_{st}.

Software compensators are mostly designed in the feed-forward mode. This eliminates the need for potential-free measurement of the inverter output voltages. Depending on the sign of the respective phase current, a fixed delay time T_{st0} is either added or not to the control signal of the half-bridge. As the actual storage delay T_{st} is not known, a complete compensation of the dead-time effect may not be achieved.

The changes of the error voltage vector $\boldsymbol{\Delta u}$ act as sudden disturbances on the current control loop. They are compensated only at the next switching of the phase leg. The remaining transient error is mostly tolerable in induction motor drive systems; synchronous machines having sinusoidal back-emf behave more sensitively to these effects as they tend to operate partly in the discontinuous current mode at light loads. The reason for this adverse effect is the absence of a magnetizing current component in the stator currents. Such machines require more elaborate switching delay compensation schemes when applied to high-performance motion control systems. Alternatively, a *d*-axis current component can be injected into the machine to shorten the discontinuous current time intervals at light loads [39].

5. Closed-loop PWM Control

Closed-loop PWM schemes generate the switching sequences inherently in a closed control loop, Fig. 6(b). The feedback loop is established either for the stator current vector or for the stator flux vector. The control is generally fast enough to compensate the nonlinear effects of pulse dropping and variable switching delay.

5.1 Nonoptimal methods

5.1.1 Hysteresis current control

The signal flow diagram in Fig. 34(a) shows three hysteresis controllers, one for each phase. Each controller determines the switching state of one inverter leg such that the error of the corresponding phase current is maintained within the hysteresis bandwidth $\pm\Delta i$. The control method is simple to implement, and its dynamic performance is excellent. There are some inherent drawbacks, though [40]:

- There is no intercommunication between the individual hysteresis controllers of the three phases and hence no strategy to generate zero voltage vectors. This increases the switching frequency at lower modulation index.

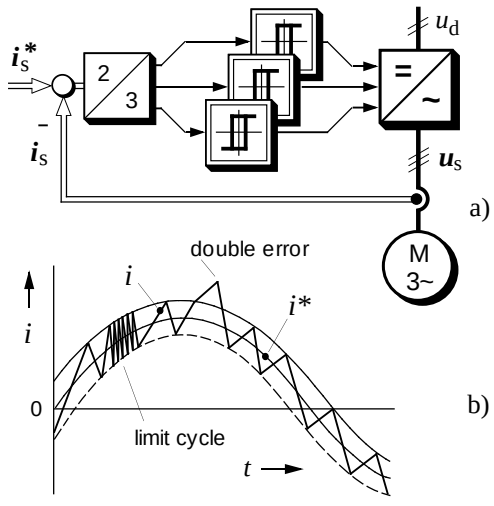

Fig. 34: Hysteresis current control; (a) signal flow diagram, (b) basic current waveform-

- There is a tendency at lower speed to lock into limit-cycles of high-frequency switching which comprise only nonzero voltage vectors (Fig. 34(b)).
- The current error is not strictly limited. The signal will leave the hysteresis band whenever the zero vector is turned on while the back-emf vector has a component that opposes the previous active switching state vector. The maximum overshoot is $2\Delta i$ (Fig. 34(b)).
- The modulation process generates subharmonic components.

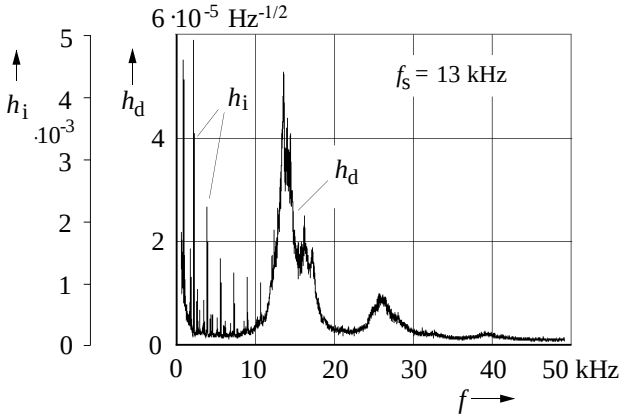

Fig. 35: Hysteresis current control; measured harmonic spectrum

The amplitude density spectrum $h_d(f)$, shown in the Fig. 35, includes also discrete components $h_i(k \cdot f_1)$ at subharmonic frequencies; it is almost independent of the modulation index. The switching frequency of a hysteresis current controller is strongly dependent on the modulation index, having a similar tendency as curve (a) in Fig. 40.

This effect can be explained with reference to Fig. 15. It is illustrated there that the current distortions reduce when the reference vector $\boldsymbol{u}^*$ reaches proximity to one of the seven switching state vectors. $\boldsymbol{u}^*$ is in permanent proximity to the zero vector at low modulation index, and in temporary proximity to an active switching state vector at high modulation index. Consequently, the constant harmonic current amplitude of a hysteresis current controller lets the switching frequency drop to near-zero at $m \approx 0$, and towards another minimum value at $m \rightarrow m_{max}$. This results in a behavior as basically demonstrated in the graph Fig. 40, showing that the switching capability of the inverter is not sufficiently utilized. The very low switching frequency in the lower modulation range favours the generation of subharmonics.

Hysteresis controllers are preferred for operation at higher switching frequency to compensate for their inferior quality of modulation. The switching losses restrict the application to lower power levels. Improvements have aimed at eliminating of the basic deficiencies of this attractive modulation technique. The current overshoot and limit cycles can be done away with at the expense of additional comparators and logic memory [41]. In an alternative approach, the hystesesis controllers process current error signals that are transformed to a rotating refrerence frame [42]. Operation at constant switching frequency can be achieved by adapting the hysteresis bandwidth. The width must be adjusted basically to the inverse function of Fig. 40(a), which implies further circuit complexity [43], [44].

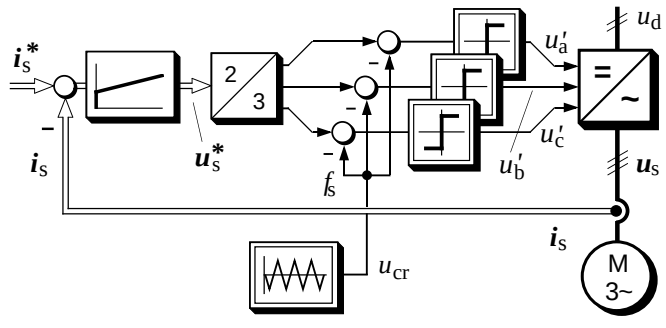

Fig. 36: Suboscillation current control, signal flow graph

5.1.2 Suboscillation current control

A carrier-based modulation scheme as part of a current control loop eliminates the basic shortcomings of the hysteresis controller. Fig. 36 shows that a proportional-intergral (PI type) controller is used to derive the reference voltage $\boldsymbol{u}^*$ for the pulsewidth modulator from the current error. The back-emf of the machine acts as a disturbance in the current control loop. This voltage is free from harmonics and discontinuities in amplitude and phase angle. It is therefore possible to compensate the influence of the back-emf through the I-channel of the PI controller. However, a steady-state tracking error will persist [45].

The tracking error is kept low by choosing a high gain for the PI-controller. The gain is limited, on the other hand, as it amplifies the harmonic currents which must not impair the proper operation of the pulsewidth modulator. This is ensured if the slope of the current error signal is always less than the slope of the triangular carrier signal.

The scheme cannot be simply looked at as a pulsewidth modulator having a superimposed current control loop. This becomes obvious when comparing its harmonic spectrum Fig. 37(a) with that of a space vector modulator, Fig. 18. The difference is explained by Fig. 37(b), which shows that the current distortions exert an influence on the switching

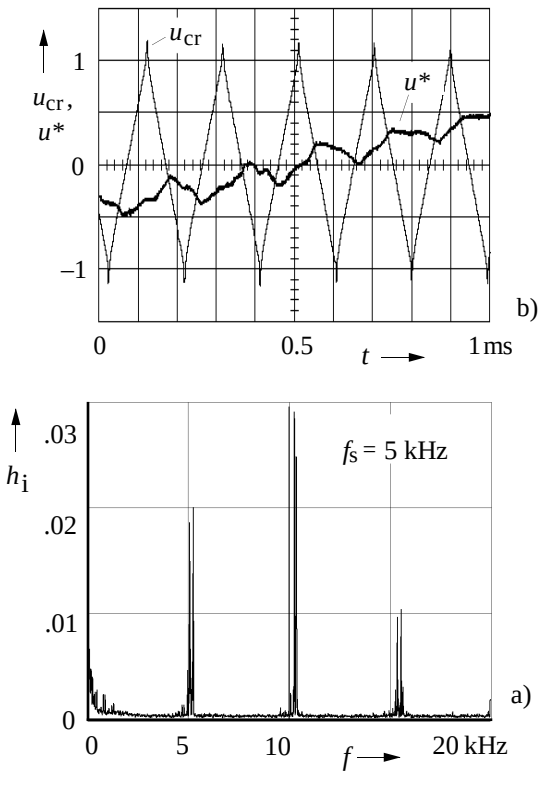

Fig. 37: Suboscillation current control; (a) harmonic spectrum, (b) carrier signal and reference signal

instants. This entails the advantage of a fast current response, provided that the modulator can react on instantaneous changes of its reference signal $\boldsymbol{u}^*$. Hence, an analogue circuit implementation of the suboscillation method is the adequate solution.

When the reference signal amplitude is driven beyond the carrier amplitude, the pulsewidth modulation is periodically interrupted and pulse dropping occurs. The beneficial effect is that the fundamental output voltage increases beyond the limit of proportional control; as compared with overmodulation techniques (Section 4.3), the harmonic distortion is higher.

5.1.3 Space vector current control

The nonzero current error in the steady-state, inherent to the previous scheme, may be undesired in a high-performance vector controlled drive. The error can be eliminated by using the back-emf voltage $\boldsymbol{u}_i$ and the leakage voltage $\sigma l_s d\boldsymbol{i}_s/dt$ of the machine as compensating feedforward signals (Fig. 38). The estimation is based on a machine model. The function of the current controller is then basically reduced to correct minor errors that originate from a mismatch of the model parameters or the model structure. The dynamic performance is improved by feedforward control based on the derivative of the current reference.

A space vector modulator is preferred in this scheme. Since its reference signal $\boldsymbol{u}^*$ is periodically sampled, Fig. 38, this signal must be free from harmonic components which may be introduced by the current feedback signal. These harmonics are eliminated by sampling the measured current signal in synchronism with the space vector modulator.

Figs. 15(b) and 15(c) show that the vector trajectory of the harmonic current passes through zero while the zero vector is on. The zero crossing occurs in the center of the zero time interval. The respective switching sequences (22) and (23) begin with one half of the zero vector time, such that each subcycle starts at zero harmonic current. The sampled current feedback signal $\boldsymbol{i}_s$ equals exactly the fundamental current $\boldsymbol{i}_{s1}$ at this time instant. The instant is predetermined by the modulator. The method requires high-bandwidth A/D conversion. Furthermore, the pulsewidth modulator must operate in synchronism with the digital algorithm computing the current controllers [19].

Note that the suboscillation method cannot provide the time instant of zero harmonic current; it is obvious from the harmonic patterns Fig. 15(b) that this time instant depends on the respective operating point and cannot be determined by a simple algorithm.

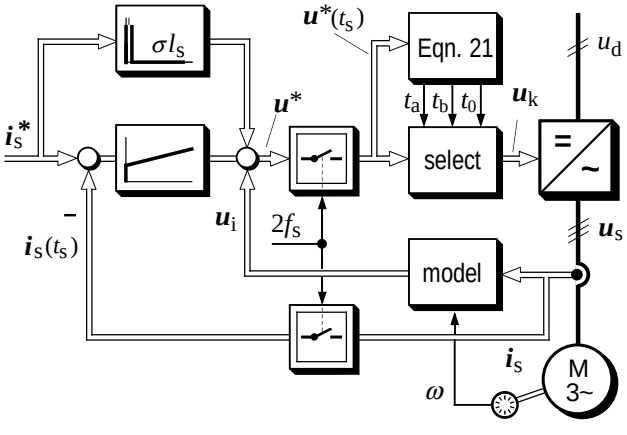

Fig. 38: Space vector current control, signal flow diagram

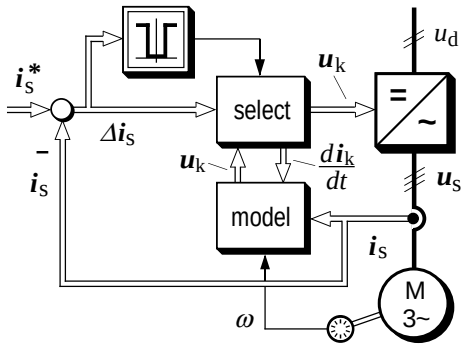

Fig. 39: Current look-up table method

5.1.4 Look-up Table Methods

In a closed-loop control scheme for a suitable space vector signal (stator current [46] or stator flux vector [47], [48]), the error is also a space vector quantity, for instance $\boldsymbol{\Delta i}(t) = \boldsymbol{i}^*(t) - \boldsymbol{i}(t)$. Limiting the magnitude $|\boldsymbol{\Delta i}|$ of this error vector, or the respective magnitudes of suitable error components, either Δi_α and Δi_β, or $\Delta\Psi_s$ and $\Delta arg(\boldsymbol{\Psi}_s)$, by predetermined boundary values is a means to terminate an actual switching state at time t_s. The next switching state vector is then read from a look-up table. The table is adressed by the error vector and other state variables, like the back-emf vector and/or the actual switching state vector (Fig. 39).

These schemes generate asynchronous pulse sequences. Since the loss factor d^2 is mostly fixed by predefined boundary conditions, the performance at varying modulation index is reflected in the switching frequency. This is demonstrated in Fig. 40(a) for a flux look-up table scheme [50].

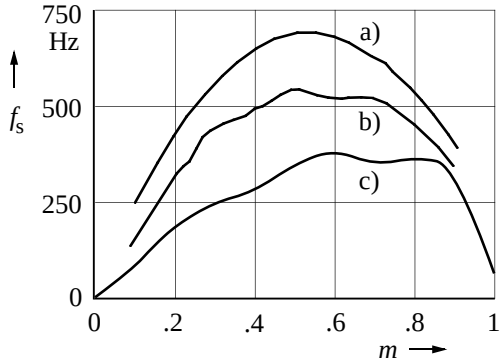

Fig. 40: Performance of nonlinear controllers; (a) flux look-up table, (b) predictive control, circular error boundary, (c) current control with field orientation

5.2 Closed-loop PWM with real-time optimization

5.2.1 Predictive current control

Pulsewidth modulation by predictive current control, Fig. 41, has common elements with the look-up table methods discussed above. In both methods, the switching instants are determined by suitable error boundaries. As an example, Fig. 42 shows a circular boundary, the location of which is controlled by the current reference vector $\boldsymbol{i}_s^*$. When the current vector $\boldsymbol{i}_s$ touches the boundary line, the next switching state vector is determined by prediction and optimization.

The trajectories of the current vector for each possible switching state are then computed, and predictions are made of the respective time intervals required to reach the error boundary again. These events depend also on the location of the error boundary, which is considered moving in the

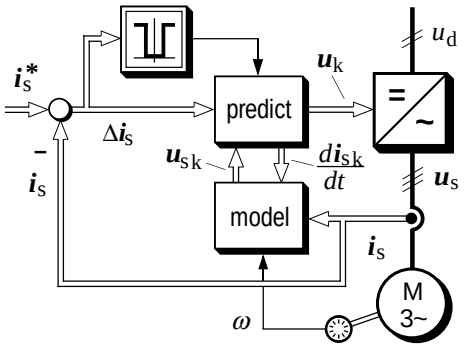

Fig. 41: Predictive current control, signal flow diagram

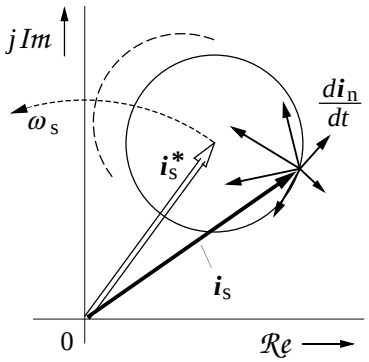

Fig. 42: Predictive current control, boundary circle and space vectors; dashed circle: boundary at the next instant of switching

complex plane as commanded by the predicted current reference. The movement is indicated by the dotted circle in Fig. 42. The predictions of the switching instants are based on a simplified mathematical model of the machine, Fig. 14. The switching state vector that produces the maximum on-time is finally selected. This corresponds to minimizing the switching frequency [49]. The optimization can be extended to include the next two switching state vectors [50].

The algorithms which determine the optimal switching state vector take about 20 µs on a DSP. Such delay is tolerable at lower switching frequency. Higher frequencies are handled by employing the double prediction method: Well before the boundary is reached, the actual current trajectory is predicted in order to identify the time instant at which the boundary transition is likely to occur. The back emf vector at this time instant is then predicted. It is used for the optimal selection of the future switching state vector using the earlier described procedure. The corresponding signals are shown in Fig. 43 [51].

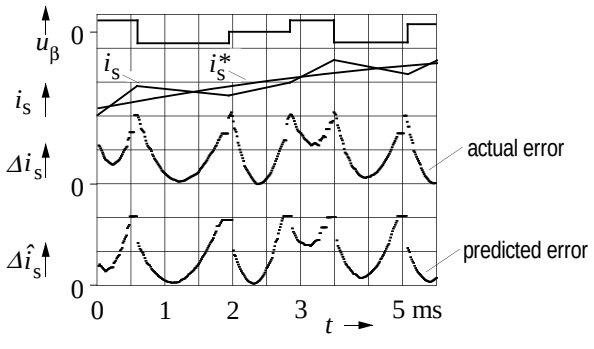

Fig. 43: Predictive current control, measured waveforms at double prediction

The performance of a predictive current control scheme which maximizes the on-durations of the next two switching state vectors is illustrated in Fig. 40(b).

5.2.2 Pulsewidth control with field orientation

A further reduction of the switching frequency, which may be needed in very-high-power applications, can be achieved by defining a current error boundary of rectangular shape, having the rectangle aligned with the rotor flux vector of the machine, Fig. 44. This transfers a major portion of the unavoidable current harmonics to the rotor-field axis where they have no direct influence on the machine torque; the large rotor time constant eliminates the indirect influence on torque through the rotor flux. The selection of the switching state vectors is based on prediction, satisfying the objectives that the switching frequency is minimized, and that switching at *d*-current boundaries is avoided to the extent possible. This can be seen in the oscillogram Fig. 44. Using a rectangular boundary area in field coordinates leads to a reduction of switching frequency over what can be achieved with a circular boundary area (Fig. 40(c)), [52].

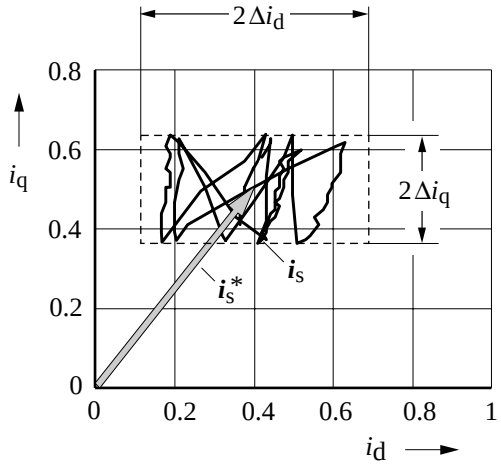

Fig. 44: Pulsewidth modulation with field orientation

5.2.3 Trajectory tracking control

The off-line optimization approach (Section 4.4) provides a global optimum under the restricting condition of steady-state operation; there is no restriction as regards the time interval of optimization, and hence all switching instants can be optimized in a closed algorithmic procedure. However, the steady-state restriction makes the dynamic performance poor, which renders such scheme nearly impracticable.

On-line methods, in contrast, target at an optimization within a restricted time interval. They rely only on the next, at maximum on the next two switching instants as the basis of optimization. Only a local optimum can be obtained, therefore. Every solution depends on the actual initial conditions, which are the outcome of the optimization in the previous time interval. A small sacrifice on the optimum criterion in one time interval might entail large benefits in the following intervals. This explains why the global optimum cannot be reached. On-line methods also fail to provide synchronous switching, which is important if the pulse number is low. Against this, the dynamic performance of on-line methods is excellent.

The combination of off-line optimization for the steady-state and on-line optimization for transient operation exploits the advantages of both methods. The concept re-

quires all steady-state current harmonic trajectories, in correspondence to the stored off-line optimized pulse sequences, be available in the modulator and used as templates for the actual current waveform. Once an optimal pulse pattern is selected, the associated steady-state trajectory is used to define a time-moving target point. The location of the target point on the trajectory is controlled by the fundamental phase angle which is also used to determine the switching instants from the actual pulse pattern. Note that it is not sufficient that the actual current just follows the template trajectory; it must exactly coincide with the moving target point on the template [53].

The approach defines a tracking problem to be solved in real-time. Fig. 45 shows the measured current trajectory of a transient process. High overcurrents occur in an off-line optimized PWM scheme (Fig. 45(a)). With the tracking control engaged (Fig. 45(b)) the dynamic current error is minimized and the optimal steady-state trajectory is reached immediately after the transient.

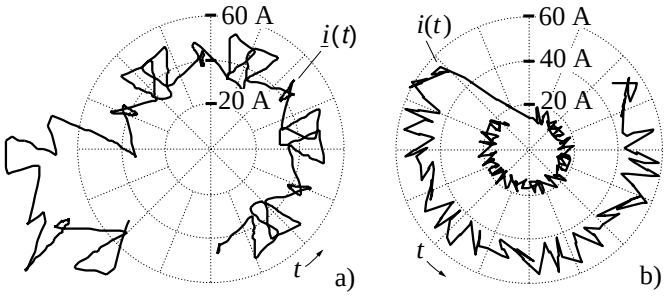

Fig. 45: Synchronous optimal PWM; a) without, b) with trajectory tracking control (different operating conditions)

6. Current Source Inverter

The preceeding discussions on pulsewidth modulation techniques made reference to a power circuit configuration as in Fig. 3, in which the dc power is delivered by a voltage source U_d. Rectangular voltage waveforms are impressed on the load circuit, from which current waveforms result that depend on the actual load impedances.

Another approach, dual to the aforementioned principle of power conversion, is the current source inverter. A switched rectangular current waveform is injected into the load, and it is the voltage waveforms which develop under the influence of the load impedances. The fundamental frequency is determined by the switching sequence, exactly as in the case of a voltage source inverter.

There are two different principles employed to control the fundamental current amplitude in a current sourve inverter. Most frequently the dc current source is varied in magnitude, which eliminates the need for fundamental current control on the ac side, and pulsewidth modulation is not required. An alternative, although not very frequently applied, consists controlling the fundamental current by pulsewidth modulation [54]. There is a strong similarity to PWM techniques for voltage source inverters, although minor differences exist.

The majority of applications are based on the voltage source principle, which is owed in the first place to favoring properties of the available power semiconductor switches.

7. Summary

Pulsewidth modulation for the control of three-phase power converters can be performed using a large variety of different methods. Their respective properties are discussed and compared based on mathematical analyses and on measured results obtained from controlled drive systems in operation.

Performance criteria assist in the selection of a PWM scheme for a particular application. An important design parameter is the switching frequency since it determines the system losses. These are hardly a constraint at low power levels, permitting high frequency switching combined with straightforward modulation methods. The important selection factors in this range are cost of implementation and dynamic performance. As the losses force the switching frequency to be low at higher power, elaborate techniques are preferred including off-line and on-line optimization. These permit that the contradicting requirements of slow switching and fast response can be satisfied.

8. References

1. P. K. Kovács, „Transient Phenomena in Electrical Machines“, *Elsevier Science Publishers, Amsterdam*, 1994.
2. E. A. Klingshirn and H. E. Jordan, „A Polyphase Induction Motor Performance and Losses on Nonsinusoidal Voltage Sources“, *IEEE Trans. Power App. Syst.*, Vol. PAS-87, pp. 624-631, March 1968.
3. J. M. D. Murphy and M. G. Egan, „A Comparison of PWM Strategies for Inverter-Fed Induction Motors“, *IEEE Trans. Industry Appl.*, Vol. IA-19, No. 3, pp. 363-369, May/June 1983.
4. J. T. Boys and P. G. Handley, „Harmonic Analysis of Space Vector Modulated PWM Waveforms“, *IEE Proc. B*, 137 (4), pp. 197-204, 1990.
5. F. C. Zach, R. Martinez, S. Keplinger and A. Seiser, „Dynamically Optimal Switching Patterns for PWM Inverter Drives“, *IEEE Trans. Industry Appl.*, Vol IA-21, No. 4, Jul./Aug. 1985, pp. 975-986.
6. T. A. Lipo, P. C. Krause and H. E. Jordan, „Harmonic Torque and Speed Pulsations in a Rectifier-Inverter Induction Motor Drive“, *IEEE Trans. Power App. Syst.*, Vol. PAS-88, pp. 579-587, May 1969.
7. T. G. Habetler and D. M. Divan, „Performance Characterization of New Discrete Pulse Modulated Current Regulator“, *IEEE Ind. Appl. Soc. Ann. Meet., Pittburgh/PA*, 1988, pp. 395-405.
8. *P519, IEEE Recommended Practices and Requirements for Harmonics Control in Electric Power Systems.*
9. W. Leonhard, „Control of Electrical Drives“, Berlin, Heidelberg - Germany, 1985.
10. A. Schönung and H. Stemmler, „Static Frequency Changers with Subharmonic Control in Conjunction with Reversible Variable Speed AC Drives“, *Brown Boveri Rev.*, pp. 555-577, 1964.
11. D. A. Grant and J. A. Houldsworth, „PWM AC Motor Drive Employing Ultrasonic Carrier“, *IEE Conf. Pow. Electronics Var. Speed Drives, London*, 1984, pp. 234-240.
12. J. W. Kolar, H. Ertl, and F. C. Zach, „Influence of the Modulation Method on the Conduction and Switching Losses of a PWM Converter System“, *IEEE Trans. Ind. Appl.*, Vol. 27, No. 6, Nov./Dec. 1991, pp. 1063-1075.
13. M. Depenbrock, „Pulsewidth Control of a 3-phase Inverter with Nonsinosoidal Phase Voltages“, *IEEE/IAS Int. Semicond. Power Conv. Conf.* Orlando/Fla. 1975, pp.399-398.
14. S. R. Bowes, „New Sinosoidal Pulsewidth Modulated Inverter“, *Proc. Inst. Elec. Eng.*, Vol. 122, Nov. 1975, pp. 1279-1285.
15. Intel User's Manual 8XC196MC, Intel Corporation 1992.
16. B. K. Bose and H. A. Sutherland, „A High-Performance Pulsewidth Modulator for an Inverter-Fed Drive System Using a Microcomputer“, *IEEE Trans. Ind. Appl.*, Vol. IA-19, No. 2, Mar./Apr. 1983, pp. 235-243.
17. S. R. Bowes and R. R. Clements, „Computer-Aided Design of PWM Inverter Systems“, *IEE Proc. B*, Vol. 129, No. 1, Jan. 1982, pp. 1-17.
18. A. Busse and J. Holtz, „Multiloop Control of a Unity Power Factor Fast-Switching AC to DC Converter“, *IEEE Pow. Elec. Special. Conf., Cambridge*, 1982, pp. 171-179.
19. G. Pfaff, A. Weschta and A. Wick, „Design and Experimental

Results of a Brushless AC Servo Drive",. *IEEE/IAS Ann. Meet., San Francisco* 1982, pp. 692-697.
20. J. Holtz, P. Lammert and W. Lotzkat, „High-Speed Drive System with Ultrasonic MOSFET PWM Inverter and Single-Chip Microprocessor Control", *IEEE Trans. Industry Appl.*, Vol. IA-23, No. 6, pp. 1010-1015, Nov./Dec. 1987.
21. J. Holtz, E. Bube, „Field Oriented Asynchronous Pulsewidth Modulation for High Performance AC Machine Drives Operating at Low Switching Frequency", *IEEE Trans. Industry Appl.*, Vol. IA-27, No. 3, pp. 574-581, May/June 1991.
22. O. Ogasawara, H. Akagi, and A. Nabae, „A Novel PWM Scheme of Voltage Source Inverters Based on Space Vector Theory", *EPE Europ. Conf. Power Electronics and Appl., Aachen,* 1989, pp. 1197-1202.
23. J. W. Kolar, H. Ertl, and F. C. Zach, „Calculation of the Passive and Active Component Stress of Three-Phase PWM Converter Systems with High Pulse Rate", *EPE Europ. Conf. Power Electronics and Appl., Aachen,* 1989, pp. 1303-1312.
24. K. Heintze, *et al.*, „Pulsewidth Modulating Static Inverters for the Speed Control of Induction Motors", *Siemens-Z.*, Vol 45 (3), 1971, pp. 154-161.
25. G. B. Kliman and A. B. Plunkett, „Development of a Modulation Strategy for a PWM Inverter Drive", *IEEE Trans. Industry Appl.*, Vol. IA-15, No. 1, pp. 702-709, Jan./Feb. 1979.
26. T. G. Habetler and D. Divan, „Acoustic Noise Reduction in Sinusoidal PWM Drives Using a Randomly Modulated Carrier", *IEEE Trans. Pow. Electr.*, Vol. 6, No. 3, pp. 356-363, July 1991.
27. J. Holtz and L. Springob, „Reduced Harmonics PWM Controlled Line-Side Converter for Electric Drives", *IEEE Trans. Ind. Appl.*, Vol. 29, No. 4, Nov. 1993, pp. 814-819.
28. J. Holtz, W. Lotzkat and A. Khambadkone, „On Continuous Control of PWM Inverters in the Overmodulation Range with Transition to the Six-Step Mode", *IEEE Pow. Elec. Special. Conf., Toledo/Spain,* 1992.
29. S. P. Jackson, „Multiple Pulse Modulation in Static Inverters Reduces Selected Output Harmonics and Provides Smooth Adjustment of Fundamentals", *IEEE Trans. Indust. and General Appl.*, Vol IGA-6, No. 4, July/Aug. 1970, pp. 357-360.
30. J. Holtz, „On the Performance of Optimal Pulsewidth Modulation Techniques", *European Power Electronics Journal* (1993), pp. 17-26.
31. H. S. Patel and R. G. Hoft, „Generalized Techniques of Harmonic Elimination and Voltage Control in Thyristor Inverters", *IEEE Trans. Industry Appl.*, Vol. IA-9, No. 3, May/June 1973, pp. 310-317.
32. G. S. Buja and G. B. Indri, „Optimal Pulsewidth Modulation for Feeding AC Motors", *IEEE Trans. Industry Appl.*, Vol. IA-13, No. 1, Jan./Feb. 1977, pp. 38-44.
33. J. Holtz, S. Stadtfeld, H.-P. Wurm, „A Novel PWM Technique Minimizing the Peak Inverter Current at Steady-State and Transient Operation", *Elektr. Bahnen,* Vol. 81, pp. 55-61, 1983.
34. F. C. Zach and H. Ertl, „Efficiency Optimal Control for AC Drives with PWM Inverters", *IEEE Trans. Ind. Appl.*, Vol. IA-21, No. 4, Jul./Aug., 1985, pp. 987-1000.
35. J. Holtz and B. Beyer, „Optimal Pulsewidth Modulation for AC Servos and Low-Cost Industrial Drives", *IEEE Ind. App. Soc. Ann. Meeting, Houston/Tx.*, 1992, pp. 1010-1017.
36. M. Mutch, K. Sakai and et al: „Stabilizing Methods at High Frequency for an Induction Motor Drives driven by a PWM Inverter", *EPE Europ. Conf. Power Electronics and Appl., Florence-Italy*, 1991, pp. 2/352-358
37. R. D. Klug, „Effects and Correction of Switching Dead-Times in 3-Phase PWM Inverter Drives", *EPE Europ. Conf. Power Electronics and Appl., Aachen*, 1989, pp. 1261-1266.
38. Y. Murai, T. Watanabe and H. Iwasaki, „Waveform Distortion and Correction Circuit for PWM Inverters with Switching Lag-Times", *IEEE Trans. Industry Appl.*, Vol. IA-23, No. 5, pp. 881-886, Sept./Oct. 1987.
39. Y. Wang, H. Grotstollen, „Control Strategies for the Discontiuous Current Mode of AC Drives with PWM Inverters", *EPE Europ. Conf. Power Electronics and Appl., Florence/ Italy*, 1991, pp. 3/217-222.
40. D. M. Brod and D. W. Novotny, „Current Control of VSI-PWM Inverters", *IEEE Trans. Industry Appl.*, Vol. IA-21, No. 3, pp. 562-570, May/June 1985.
41. S. Salama, S. Lennon, „Overshoot and Limit Cycle Free Current Control Method for PWM Inverter", *EPE Europ. Conf. Power Electronics and Appl., Florence/Italy*, 1991, pp. 3/247-251.
42. J. Rodriguez and G. Kastner, „Nonlinear Current Control of an Inverter-Fed Induction Machine". *ETZ Archiv,* 1987. pp. 245 - 250.
43. L. Malesani and P. Tenti, „A Novel Hysteresis Control Method for Current-Controlled VSI-PWM Inverters with Constant Modulation Frequency", *IEEE Ind. Appl. Soc. Ann. Meet.*, 1987, pp. 851 - 855.
44. B. K. Bose, „An Adaptive Hysteresis-Band Current Control Technique of a Voltage-Fed PWM Inverter for Machine Drive System", *IEEE Trans. Ind. Electron., Vol. 37., No.5,* Oct. 1990, pp. 402 - 408.
45. V. R. Stefanovic, „Present Trends in Variable Speed AC Drives", *Int. Pow. Elec. Conf. IPEC Tokyo*, 1983, pp. 438-449.
46. A. Nabae, S. Ogasawara and H. Akagi, „A Novel Control Scheme for PWM Controlled Inverters", *IEEE Ind. Appl. Soc. Ann. Meet., Toronto,* 1985, pp. 473-478.
47. V. G. Török, „Near-Optimum On-Line Modulation for PWM Inverters", *IFAC Symp., Lausanne*, 1983, pp.247-254.
48. I. Takahashi and N. Toshihiko, „A New Quick-Response and High-Efficiency Control Strategy of an Induction Motor", *IEEE Ind. Appl. Soc. Ann. Meet., Toronto,* 1985, pp. 820-827.
49. J. Holtz and S. Stadtfeld, „A Predictive Controller for the Stator Current Vector of AC Machines Fed from a Switched Voltage Source", *IPEC Tokyo*, 1983, pp. 1665-1675.
50. U. Boelkens, „Comparative Study on Trajectory-Based Pulsewidth Modulation Methods for Three-Phase Converters Feeding Induction Machines", *Ph.D.-Thesis* (in German), *Wuppertal University*, 1989.
51. J. Holtz and S. Stadtfeld, „A PWM Inverter Drive System with On-Line Optimized Pulse Patterns", *EPE Europ. Conf. Power Electronics and Appl., Brussels,* 1985, pp. 3.21-3.25.
52. A. Khambadkone and J. Holtz, „Low Switching Frequency High-Power Inverter Drive Based on Field-Oriented Pulsewidth Modulation", *EPE Europ. Conf. Power Electronics and Appl., Florence/Italy*, 1991, pp. 4/672-677.
53. J. Holtz and B. Beyer, „The Trajectory Tracking Approach - A New Method for Minimum Distortion PWM in Dynamic High-Power Drives". *IEEE Ind. Appl. Soc. Ann. Meet., Houston/Tx.*, 1992, pp. 331-338.
54. G. Amler, „A PWM Current-Source Inverter for High Quality Drives", *EPE Journal*, Vol 1, No.1, July 1991, pp. 21 32.